

Review

High-Entropy Materials: Features for Lithium–Sulfur Battery Applications

Yikun Yao, Jiajun Chen, Rong Niu, Zhenxin Zhao and Xiaomin Wang *

College of Materials Science and Engineering, Taiyuan University of Technology, Taiyuan 030024, China

* Correspondence: wangxiaomin@tyut.edu.cn

Abstract: The emergence of various electronic devices and equipment such as electric vehicles and drones requires higher energy density energy storage devices. Lithium–sulfur batteries (LSBs) are considered the most promising new-generation energy storage system owing to its high theoretical specific capacity and energy density. However, the severe shuttle behaviors of soluble lithium polysulfides (LiPSs) and the slow redox kinetics lead to low sulfur utilization and poor cycling stability, which seriously hinder the commercial application of LSBs. Therefore, various catalytic materials have been employed to solve these troublesome problems. High entropy materials (HEMs), as advanced materials, can provide unique surface and electronic structures that expose plentiful catalytic active sites, which opens new ideas for the regulation of LiPS redox kinetics. Notwithstanding the many instructive reviews on LSBs, this work aims to offer a complete and shrewd summary of the current progress in HEM-based LSBs, including an in-depth interpretation of the design principles and mechanistic electrocatalysis functions, as well as pragmatic perspectives.

Keywords: lithium–sulfur batteries; catalysis; high-entropy materials; active sites

1. Introduction



Citation: Yao, Y.; Chen, J.; Niu, R.; Zhao, Z.; Wang, X. High-Entropy Materials: Features for Lithium–Sulfur Battery Applications. *Metals* **2023**, *13*, 833. <https://doi.org/10.3390/met13050833>

Academic Editor: Branimir N. Grgur

Received: 28 February 2023

Revised: 17 March 2023

Accepted: 28 March 2023

Published: 24 April 2023



Copyright: © 2023 by the authors. Licensee MDPI, Basel, Switzerland. This article is an open access article distributed under the terms and conditions of the Creative Commons Attribution (CC BY) license (<https://creativecommons.org/licenses/by/4.0/>).

The widespread use of traditional fossil fuels and various emerging electronic devices and equipment such as electric vehicles and drones make finding higher energy density energy storage devices to replace traditional energy systems urgent [1–4]. Lithium–sulfur batteries (LSBs) have garnered much attention due to its high theoretical energy density, 2600 Wh kg^{-1} , and theoretical specific capacity, 1675 mAh g^{-1} [5]. In addition, natural reserves of active material sulfur are inexpensive and environmentally friendly [6]. The above advantages have also attracted extensive attention and research on LSBs by domestic and foreign researchers [7]. However, the insulating property of sulfur, the sluggish redox kinetics of $\text{Li}_2\text{S}_2/\text{Li}_2\text{S}$, the shuttle effect of soluble lithium polysulfides (LiPSs), and the huge volume change during lithiation/delithiation are not conducive to achieving high utilization of active S and a long cycle lifespan [8–11].

In order to tackle the above critical obstacles, researchers have extensively investigated the performance improvement of LSBs mainly from four aspects: sulfur cathodes, electrolytes, separators, and Li anodes [12–15]. Figure 1 depicts the reaction mechanism of the interconversion of S_8 and LiPSs during charging and discharging, explaining the reasons for the slow reaction kinetics and the mechanism of catalytic LiPS conversion. Physical confinement and chemical adsorption strategies are common strategies for inhibiting the diffusion of LiPSs [16]. However, high sulfur loading cannot be achieved due to the limited adsorption sites. Accelerating redox reactions is another effective method to restrain the migration of LiPSs [17]. Recently, catalysis has been proposed for accelerating the conversion of soluble LiPSs to solid products and reducing their accumulation on electrolytes [18]. Undoubtedly, once sulfur host materials with strong adsorption and fast catalytic conversion of LiPSs are synthesized, the inhibition of the shuttle problem and an improvement in the redox kinetics of LiPSs can be achieved simultaneously. Therefore, it is imperative to explore new catalytic hosts for achieving high-energy-density LSBs.

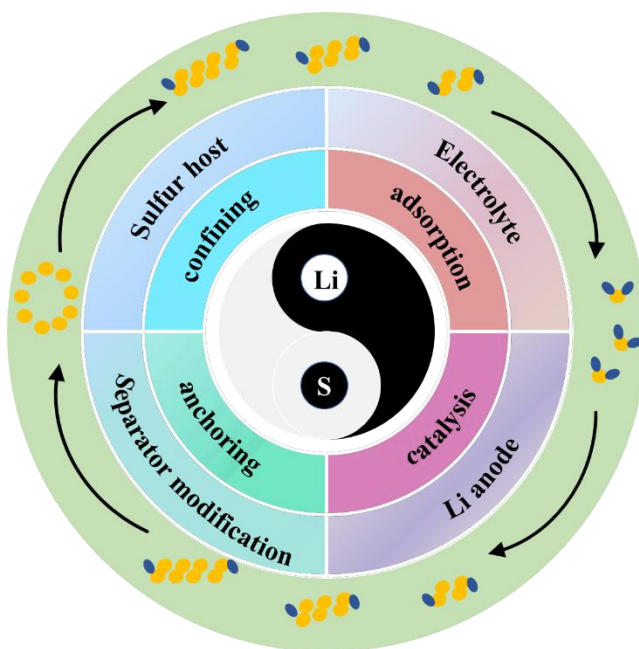


Figure 1. An overview of the main components of LSBs, the key pathways for limiting LiPSs, and the material changes during charging and discharging.

In view of LiPSs being negatively charged polar substances, as a Lewis base, they can provide Lewis acids with excess electron pairs to form coordination bonds. Metal atoms with abundant polar sites can be strongly bonded to LiPSs through Lewis acid-base interactions, polar–polar interactions, and sulfur-chain catenation, thus anchoring and trapping them to the host surface and reducing the loss of active substances [19,20]. However, single-compound catalysts cannot balance the adsorption and desorption of LiPSs, resulting in poor catalytic activity [21]. Therefore, catalysts with multiple anchoring and catalytical active centers are needed to provide a proper adsorption capacity for LiPSs and to accelerate its conversion. In addition, the research on conventional catalysts has mainly focused on binary/ternary metal nanoalloys. On the one hand, the modulation of its electronic structure and the improvement in its catalytic performance are constrained [22]. On the other hand, the composition changes during the catalytic process due to the low atomic diffusion potential [23]. Therefore, the current binary/tertiary alloys can no longer meet the requirements of advanced catalysis [24].

Based on this, high-entropy materials (HEMs), consisting of a good mixture of five or more major component atoms/molecules, have also attracted a lot of attention as potential candidates as multicomponent catalysts that achieve strong synergistic effects [25]. In this review, we focus on the major development of HEMs as host materials, explaining its design principles, structure and properties, and electrochemical performances. Finally, some future perspectives and directions are pointed out based on the literature, which focus on further progress in LSBs.

2. High-Entropy Materials

2.1. The Concept of High Entropy

“Entropy” is a thermodynamic parameter that indicates the degree of disorder in a system. The higher the degree of disorder in the system, the higher the entropy. The concept of “high entropy” originally came from high-entropy alloys (HEAs). Yeh et al. [26] and Cantor et al. [27] proposed the concept of “HEAs” in 2004. HEAs, unlike conventional alloys, are usually composed of five or more elements in equal or nearly equal atomic ratios, with 5–35% of each element [28]. HEAs have attracted much interest in the development and application of electro/thermal catalytic clean energy conversion due to their unique microstructure, excellent thermal stability, and catalytic activity for various reactions.

The entropy of a configuration increases with the number of elements, which is known as the high-entropy effect, and it can greatly enhance the stability of the material [29]. As shown in Figure 2, the high-entropy effect is manifested in four main ways [30]: (1) In the thermodynamic high-entropy effect, N-element alloy systems can form up to $N + 1$ phases. However, HEAs tend to form single-phase solid solutions rather than split phases or various intermetallic compounds. (2) In the lattice distortion effect of the structure, for HEA, the individual atoms are randomly distributed in the crystal dot matrix; the radii and chemical bonds of different atoms differ greatly; and the environment around each atom as well as the occupancies are different, which makes the lattice interior have greater lattice distortion and defects than conventional alloys [31]. (3) In the hysteresis diffusion effect of kinetics, precipitates below the tens of nanometer scale are often observed in the interior of HEA, which is not easily found in conventional alloys, indicating that the diffusion and phase transformation rates are very slow in HEA, and they are not susceptible to structural changes such as grain coarsening or recrystallization at high temperatures. (4) In the “cocktail” effect on properties, the basic properties of different components and their interactions make the HEMs present more complex properties.

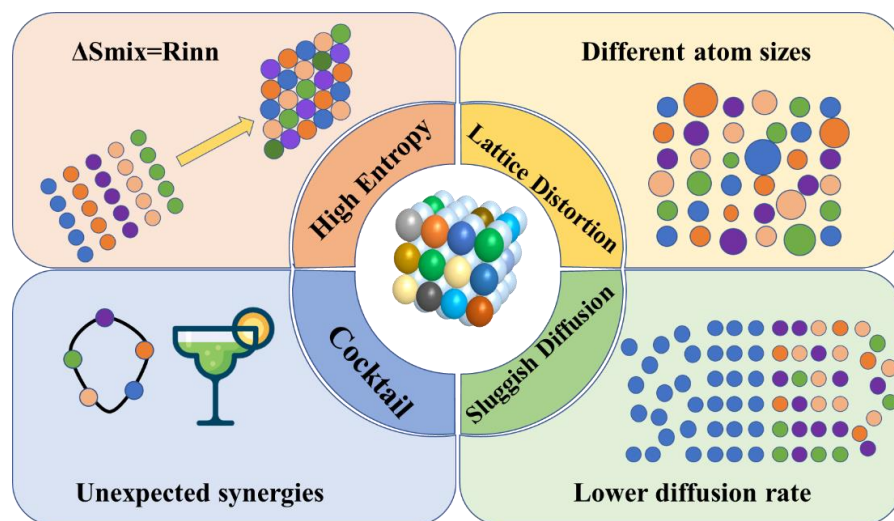


Figure 2. Four effects of high-entropy materials.

Following HEAs, inspired by breakthroughs in metal clusters, the concept of an HEM design has been extended to high-entropy oxides (HEOs), high-entropy ceramics (HECs), high-entropy polymers (HEPs), and high-entropy composites (HECOMPs) [32]. Similar to HEAs, all HEMs are long-range ordered in terms of structure but disordered on composition. High-entropy oxides (HEOs), as a new concept, have been introduced to develop advanced materials with unique properties, which are not possible with conventional materials relying on only one or a few major elements. HEOs are multi-component oxides with a single solid solution structure composed of five or more oxides in equal or nearly equal amounts of matter, including transition metal-based HEOs (TM-HEOs), rare-earth-based HEOs (RE-HEOs), and hybrid-based HEOs (TM-RE-HEOs) [33]. HEOs represent multi-element metal systems that can crystallize in a single phase, and different systems can have different crystal structures, which can also be classified rock salt, fluorite, chalcocite, spinel, and other oxides [34].

In the past five years, high-entropy ceramic materials have sprung up gradually. Compared with HEAs, the emergence of high-entropy ceramics (HECs) provides more opportunities for the optimization of material properties and overcomes bottlenecks in material applications. HECs have good high-temperature strength, excellent creep resistance, good thermal/environmental stability, and low thermal conductivity [35]. Compared with traditional ceramic materials, HECs exhibit superior corrosion resistance, oxidation

resistance, thermal stability, and high hardness and have great potential for applications in the fields of defense and military, aerospace, and new energy.

HEAs and other HEMs have potential development abilities and broad application prospects, resulting from their unique design strategies and unique properties. As shown in Figure 3, for example, the NH_3 decomposition reaction [36], the hydrogen evolution reaction (HER) [37], lithium–sulfur batteries (LSBs), the oxygen reduction reaction (ORR) [38], the methane oxidation reaction (MOR) [39], the formic acid oxidation reaction (FAOR) [40], the CO oxidation reaction [41], the methanol oxidation reaction [42], electromagnetic wave shielding materials [43], functional coating and antibacterial materials, hydrogen storage materials, anti-radiation materials, thermoelectric materials, etc., which are expected to be widely used in various new fields.

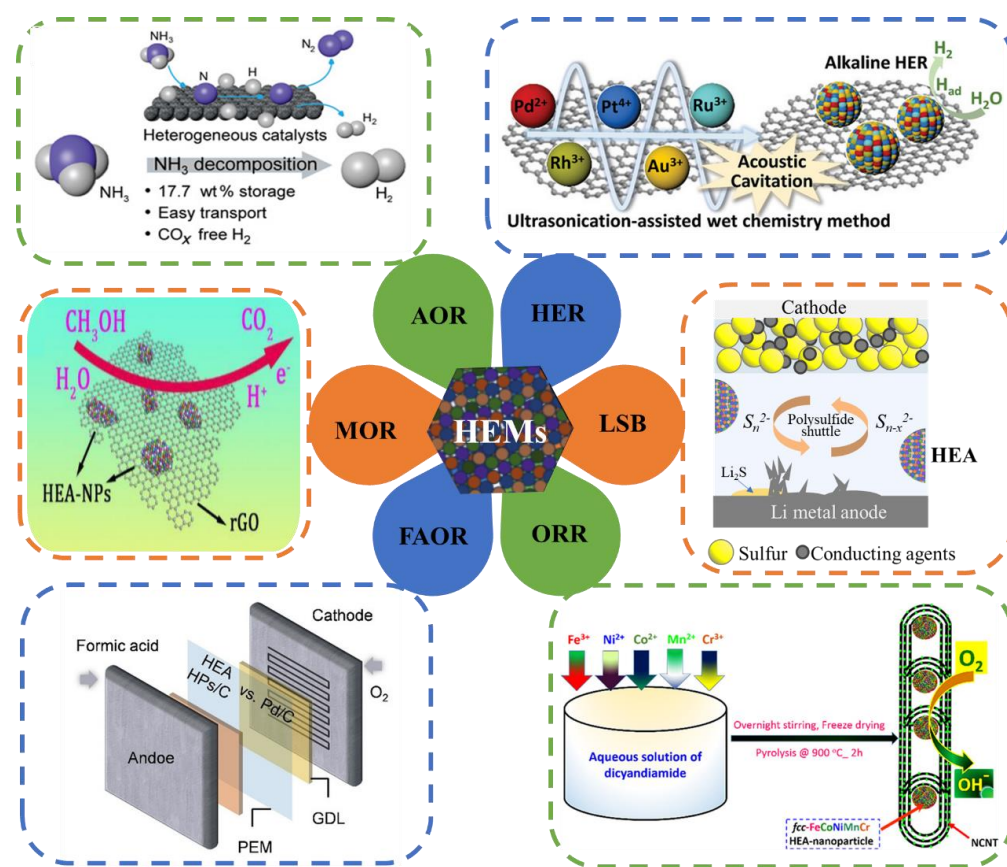


Figure 3. Six catalytic reactions of HEA-NPs. The six catalytic applications include the NH_3 decomposition reaction [36], the hydrogen evolution reaction (HER) [37], lithium–sulfur batteries (LSBs), the oxygen reduction reaction (ORR) [38], the methane oxidation reaction (MOR) [39], and the formic acid oxidation reaction (FAOR) [40].

2.2. Preparation of High-Entropy Materials

The method of synthesis of the material plays an important role in its development. Selecting a suitable synthetic route requires consideration of several aspects, such as phase stability, element distribution, morphology characteristics, desired properties, and applications. Several other parameters should be considered in the selection of the synthetic process, such as time, temperature, and complexity of the process [44]. Although large bulk and thin films are important for mechanical and coating applications, there is a general trend toward synthesizing high-entropy nanomaterials, including nanoparticles, nanofibers, nanotubes, nanosheets, etc. These nanomaterials exhibit better physical and chemical properties in some specific applications due to their core effects such as small size effect, surface effect, quantum size effect, quantum tunneling effect, and dielectric confinement effect.

Nano-HEAs are promising for a wide range of applications in multiphase catalysis [45,46]. Compared with conventional low-entropy nanomaterials, the strain effect induced by their lattice distortion has a promoting catalytic activity effect, which can lead to more stable crystal structures in arms of thermodynamics ($\Delta G_{\text{mix}} = \Delta H_{\text{mix}} - T\Delta S_{\text{mix}}$) and kinetics (vacancy mechanism for diffusion). Therefore, the design of HEA nanomaterials with specific structures provides a new research direction for the construction of efficient and stable electrocatalytic materials.

The preparation of HEMs with special morphology and controllable structure accounts for an ultimate pursuit in practical implementation. For LSBs, the synthesis of HEMs has an important impact on both their ability to confine LiPSs and superior catalytic activity. Therefore, it is worth concluding the current preparation routes for targeted HEMs. The typical methods for HEMs synthesis are discussed in the following (Figure 4):

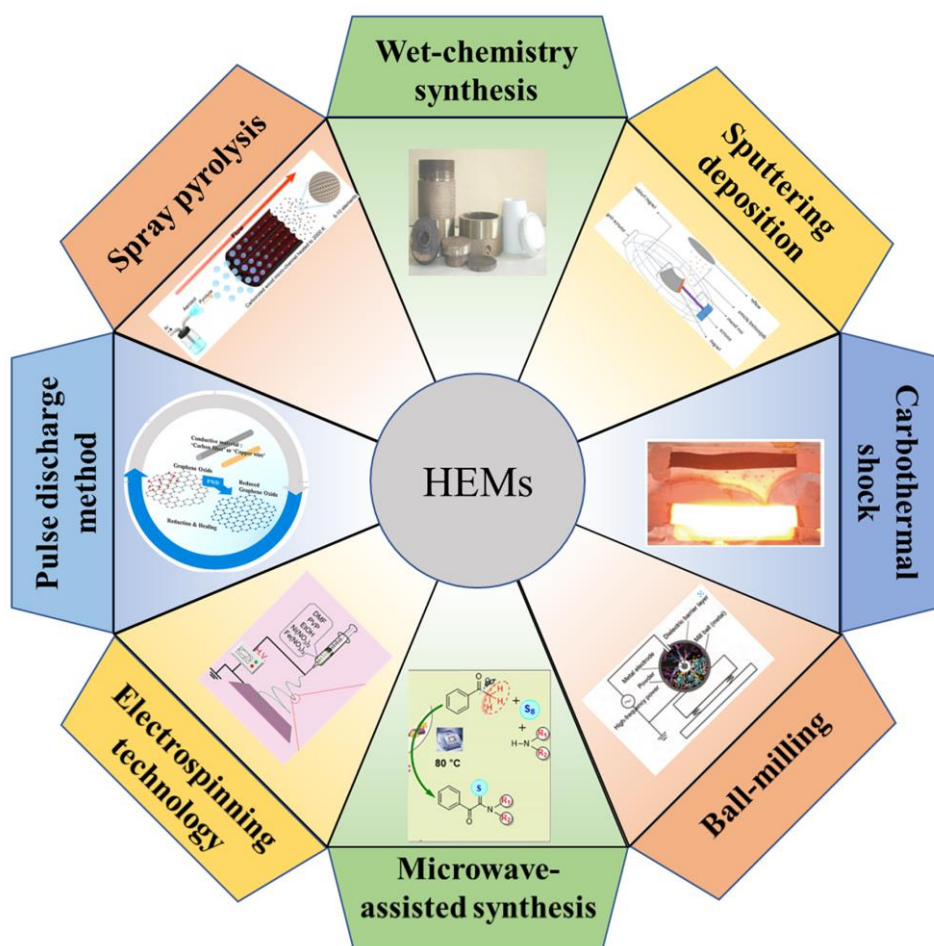


Figure 4. Common synthesis methods for high-entropy materials: wet-chemistry synthesis, sputtering deposition [47], carbothermal shock [48], ball-milling [49], microwave-assisted synthesis [50], electrospinning technology [51], pulse discharge method [52], and spray pyrolysis [53].

2.2.1. Wet-Chemistry Synthesis

Currently, traditional wet chemical synthesis methods including hydrothermal and solvothermal methods are based on the crystallization process of substances [54]. Both methods need to be carried out in a reactor. In the hydrothermal method, the reactants are dissolved in water, while it should be dissolved in an organic solvent in the solvothermal method. The morphology and particle size of the product can be influenced by temperature, pH, and reactant concentration. This is an inexpensive way to prepare high-purity, high-quality nanoparticles at low temperatures. For HEMs, the application of this method does

not have the problems of complex reaction equipment, complicated preparation processes, high reaction temperatures, and large particle sizes compared with other methods [55,56].

Jiang et al. [57] synthesized a high-entropy metal hydroxymethoxy-based material FeCoNiMgCr(OH)(OCH₃) (denoted as FeCoNiMgCr-HM) using a one-step solvothermal method to investigate the application of HEM for electrochemical water splitting. As shown in Figure 5a, the electrochemically activated FeCoNiMgCr-HM exhibited excellent catalytic properties due to the synergistic effect of the five metal cations and methoxy-induced surface reconstruction. Wu et al. [58] first synthesized six platinum-group-metal HEA nanoparticles (PGM-HEA) using simple wet chemistry. The HEA NPs are promising catalysts for complex reactions due to their various active sites and high stability. The various elements are uniformly distributed as seen in the corresponding EDS plots (Figure 5b).

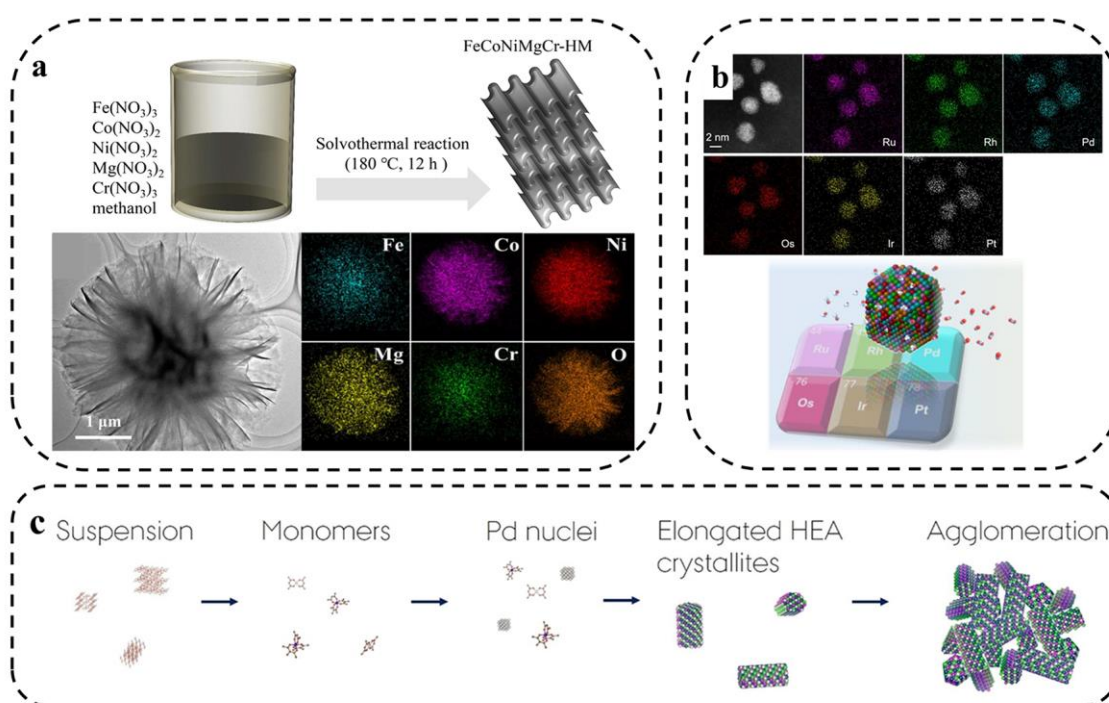


Figure 5. (a) Synthesis of high-entropy hydroxy-methoxy compounds with layered structures by one-step solvothermal method and TEM images [57]. (b) HAADF-STEM image of the as-prepared PGMHEA and the corresponding EDX maps [58]. (c) Schematic diagram of formation mechanism of PtIrPdRhRu HEA nanoparticles under solvothermal conditions [59].

Broge and coworkers [59] used the solvothermal method to synthesize PtIrPdRhRu HEAs. Homogeneous materials were obtained within a relatively narrow temperature window of about 200 °C, which is well below the reduction temperature of some metals in the solvothermal reaction of a single precursor (Figure 5c).

2.2.2. Mechanical Ball-Milling

The solid-state reaction method is a traditional method of preparing HEMs and is based on controlling the interdiffusion of the initial precursor powders to produce HEMs [60,61]. The most commonly used solid-phase reaction method is mechanical alloying, also known as mechanical ball-milling, which is commonly used to prepare metal powders. Metal powders are deformed, cold-welded, and broken in a ball mill to finally make elements to achieve atomic-level alloying. This complex and tedious physical process is mechanical alloying. The principle is shown in Figure 6a, where the sample is placed in a bowl together with the grinding balls and then violently rotated or vibrated. The collision of the ball with the bowl and the powder leads to a solid-state reaction [62]. The main

advantage of mechanized alloying is that a more uniform nanoscale tissue distribution can be obtained.

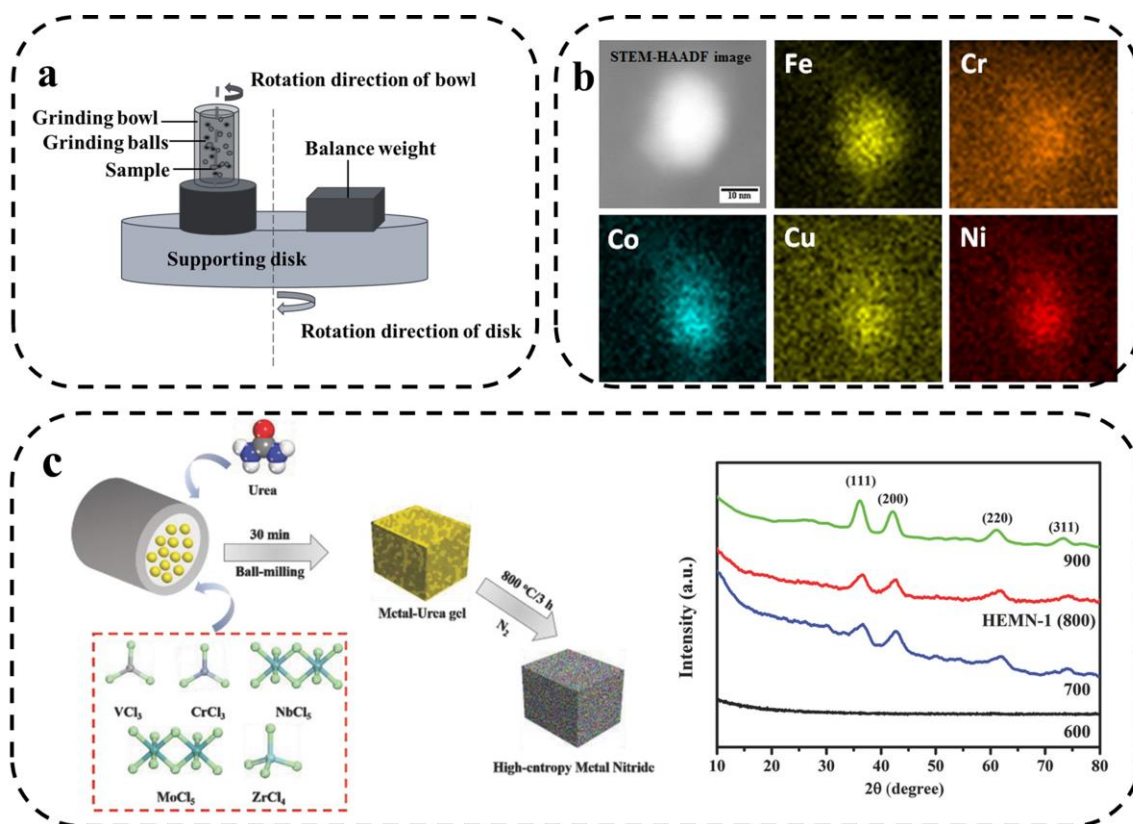


Figure 6. (a) Schematic diagram of mechanical alloying principle. (b) Representative compositional mapping result obtained from a nanoparticle [63]. (c) Two-step synthetic strategy and XRD patterns of HEMNs pyrolyzed at 600, 700, 800 (HEMN-1), and 900 °C [64].

M.Y. Rekha et al. reported the synthesis of multi-component NiFeCrCoCu HEA nanoparticle-graphene composites using mechanical ball-milling and ultrasound-assisted exfoliation methods [63]. As shown in Figure 6b, the five transition metals are uniformly distributed. Jin et al. [64] prepared a new class of high-entropy metal nitrides (HEMNs) via a two-step mechanochemical synthesis. As shown in Figure 6c, the five transition metal chlorides were mixed with urea in a ball-milling process to produce highly dispersed precursors, which were subsequently pyrolyzed under N₂ conditions. The use of five metal elements significantly increased the conformational entropy. In addition, Hari Prasad et al. [65] prepared FeNiCoCrAlMn HEA containing dispersed alumina using mechanized synthesis. The results show that the dispersion of alumina had no effect on the organization of the alloy. Both alloys have FCC and BCC biphasic structures and contain a small number of Mn₃Co₇ phases.

2.2.3. Sputtering Deposition

Sputtering includes reactive radio frequency (RF) magnetron sputtering, direct current (DC) sputtering, and multi-metal co-sputtering, which can be used to prepare hard, corrosion-resistant, high-entropy nitride, carbide, and oxide films. Sputtering deposition is a widely used technique for depositing nanoparticles or thin films on substrate materials [66]. As shown in Figure 7a, the principle of the technique is to change the metallic surface state of the target, using the interaction of equal ions in the gas under the action of electric and alternating magnetic fields. The accelerated high-energy particles bombard the target surface, and after energy exchange, the atoms on the target surface escape from the original lattice, transfer to the substrate surface, and form a film [67]. Due to the high

ability of atoms deposition, the formed film has a uniform and dense organization and a high bond with the substrate. In addition, composition control is easily ensured in the preparation of alloy films. However, the sputtering deposition speed is not quick, and the presence of radiation and bombardment of the plasma on the substrate can not only cause substrate heating but also may form internal defects.

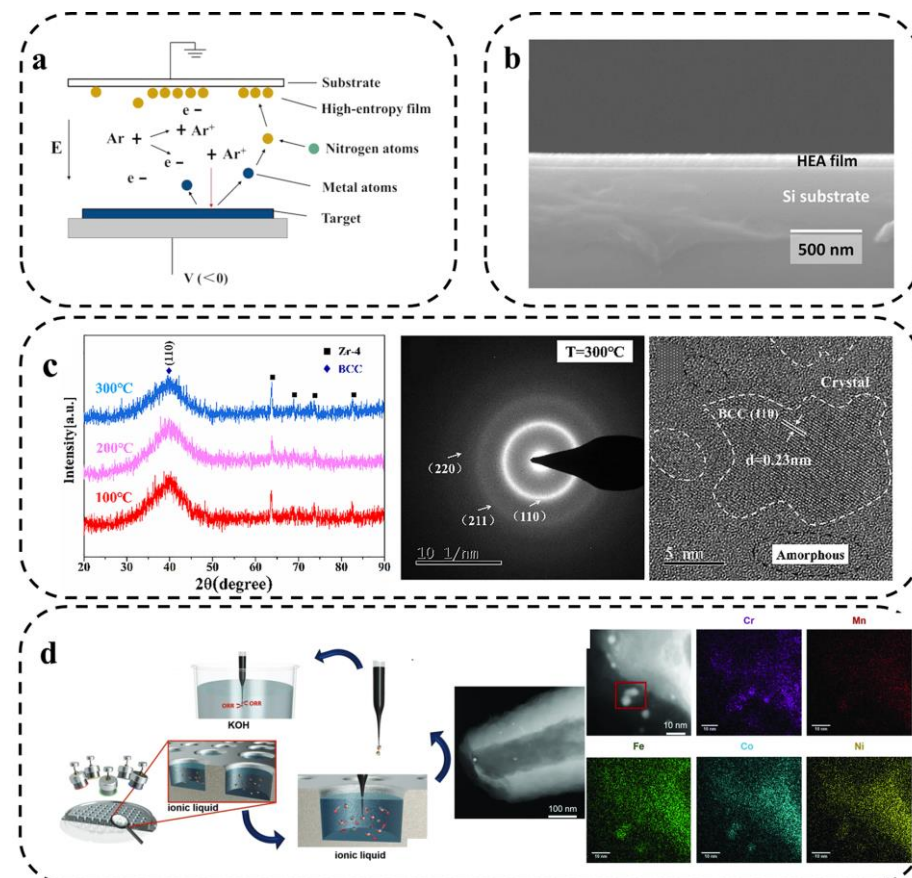


Figure 7. (a) Principle of sputtering deposition [67]. (b) Cross-sectional FE-SEM image of the ASD film [68]. (c) XRD patterns of the TiVZrCrAl coatings at different deposition temperatures, SAED pattern of the TiVZrCrAl coating deposited at 300 °C, cross sectional HRTEM image of the TiVZrCrAl coating [69], and (d) preparation of HEA NPs by combined ionic liquid co-sputtering [70].

Talluri et al. [68] performed thin film deposition using eutectic HEA ($\text{AlCoCrFeNi}_{2.1}$) as a target material using the radio frequency magnetron sputtering technique. The cross-sectional field emission scanning electron microscopy (FE-SEM) images of the generated films are shown in Figure 7b. The results show that the thickness of the film is about 95 nm, which is already in the range of nanocrystals. He et al. [69] used the magnetron sputtering method to prepare high-hardness TiVZrCrAl HEA coatings and investigated their organization, and mechanical and corrosion properties. As shown in Figure 7c, Selected area electron diffraction (SAED) maps at 300 °C showed one stronger diffraction ring and three weaker diffraction rings. The wider and weaker diffraction rings indicate that the coating is less crystalline and close to an amorphous structure, which is consistent with the XRD analysis results.

Tobias et al. [70] synthesized CrMnFeCoNi nanoparticles using magnetron sputtering, exhibiting a high entropic effect promoting the formation of a single solid solution. As shown in Figure 7d, they bombarded the elemental target with Ar plasma and sputtered the metal atoms in the target into the ionic liquid instead of the matrix. These metal atoms are subsequently nucleated and grown in the ionic liquid to generate the corresponding HEA NPs. The specific synthesis method based on combined co-sputtering from the elemental

target to the ionic liquid achieves precise tuning of the elemental composition of the multi-components alloy NPs. It was found that the material is comparable to Pt in terms of ORR activity. In addition, the size of NPs can be adjusted by choosing a suitable ionic liquid as a stabilizer and suspension medium [71].

2.2.4. Carbothermal Shock Method

Carbothermal shock (CTS) provides a new way to synthesize high-entropy nanoparticle with narrow particle size distribution and uniform dispersion. CTS is a novel ultrafast, high-temperature process (>2000 K) for the production of uniform, monodisperse HEA-NPs on conductive materials [72]. The high temperature causes rapid thermal decomposition of the metal salt precursors to form small droplets of multi-metallic solutions. Subsequently, these droplets rapidly cool and crystallize into homogeneous alloy nanoparticles independent of agglomeration, elemental segregation, or phase segregation. However, the size of the substrate conductive material is limited to a large extent, which restricts the mass production [73]. This CTS method opens up a wide scope for the synthesis of alloys and nanocrystals.

The basic principles of the CTS method have been described by Hu et al. [74] and Lu et al. [75] (Figure 8a,b). The high temperature, combined with the catalytic activity of the liquid metal, drives the rapid “fission” and “fusion” events of the particles, resulting in a homogeneous mixing of multiple elements [76]. The cooling rate can be adjusted by changing the input parameters, which greatly affects the structure of the formed nanoparticles. Compared with the conventional method, CTS could be a feasible way to form highly dispersed nanoparticles and can easily obtain nanostructured catalysts with poly-metallic compositions. It exhibits higher structural and chemical stability compared with conventionally synthesized nanocatalysts.

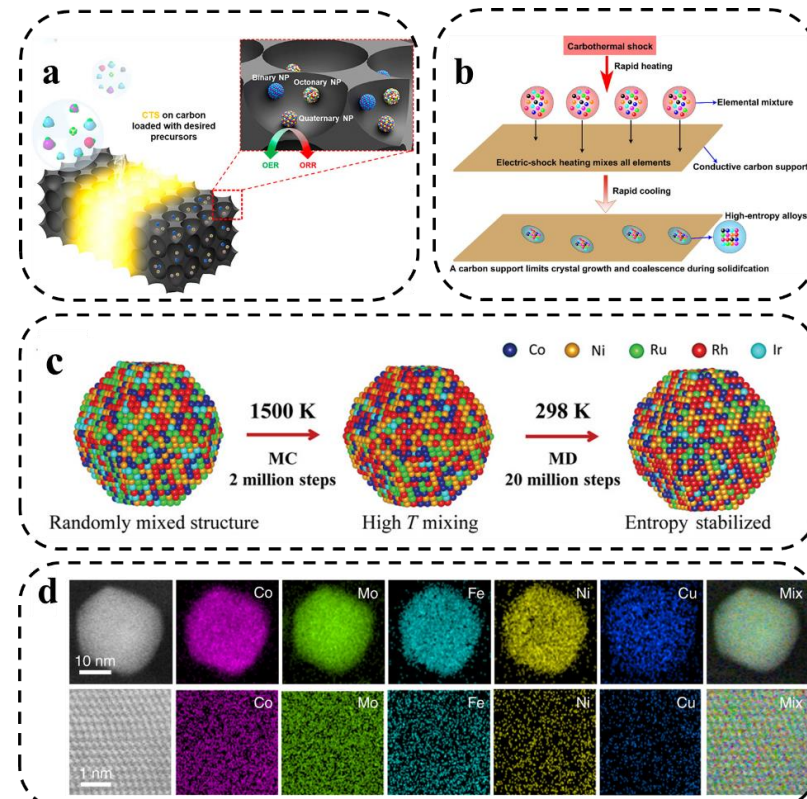


Figure 8. (a) Schematic representation of the process and capabilities of the CTS synthesis method [74]. (b) The synthesis route of nanoscale HEAs by making a mixture of many elements [75]. (c) Kinetic

formation simulation of MEA-NPs. (The hybrid Monte Carlo and molecular dynamics (MC-MD) approach. MD-MC simulation approach for the formation of an Ru-5 MEA-NP at 1500 K. The high temperature promotes uniform mixing, while the high entropy stabilizes the structure [36]). (d) STEM-based elemental maps of the HEA-Co25Mo45 nanoparticles at low (upper panel) and high (lower panel) resolutions [48].

Xie et al. [48] synthesized CoMoFeNiCu HEA NPs via rapid heating and cooling of metal precursors on oxygenated carbon carriers using the carbothermal shock method. Moreover, the mixed-phase limitation of the bimetallic CoMo alloy was broken by adjusting the ratio of Co/Mo elements in the HEA NPs. The obtained knowledge was combined with the reaction kinetics and simulated atomic structures of HEA catalysts to further explore the catalytic enhancement mechanism of HEA catalysts for efficient decomposition of ammonia. Recently, Deng [77] used nickel foil as a carrier for fast Joule heating for the ultrafast synthesis of high-entropy oxides. The method exhibits an extremely short synthesis time and wide generalizability in the synthesis of HEOs.

2.2.5. Electrospinning Technology

Electrospinning is a simple and scalable method for preparing nanofibers with controlled morphology and composition, which has played a vital role in the field of constructing one-dimensional nanostructured materials with the potential to synthesize fiber-like HEM [78]. The schematic diagram of electrospinning is presented in Figure 9A, where a precursor solution containing five metal salts is added to the needle of an electrospinning machine, and the droplets at the tip of the needle change from a sphere to a cone (i.e., a “Taylor cone”) under the action of an electric field, and the fiber filaments are obtained by extending from the tip of the “Taylor cone”. On the other side, a rotating roller receives it evenly.

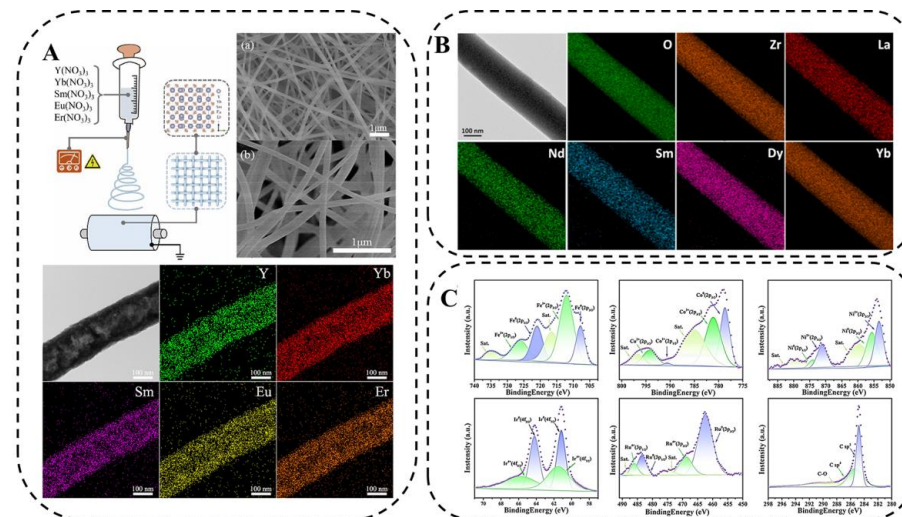


Figure 9. (A) Schematic diagram of electrospinning, SEM image of precursor of $(Y_{0.2}Yb_{0.2}Sm_{0.2}Eu_{0.2}Er_{0.2})O_3$ nanofibers and after $500\text{ }^\circ\text{C}$ calcination, and EDS images [78]. (B) Typical nanofibers and composition spectra of HE- $RE_2Zr_2O_7$ nanofibers sintered without insulation at $1000\text{ }^\circ\text{C}$ [79]. (C) XPS spectra of FeCoNiIrRu/CNFs [80].

To demonstrate the feasibility of the low-temperature synthesis of high-entropy ceramic nanofibers (HECNFs) by electrospinning, Xing [78] synthesized high-entropy $(Y_{0.2}Yb_{0.2}Sm_{0.2}Eu_{0.2}Er)O_{0.223}$ nanofibers via a new electrospinning method and low-temperature solid-solution treatment. Li [79] proposed a method for the facile preparation of high-entropy ceramic nanofibers $(La_{0.2}Nd_{0.2}Sm_{0.2}Dy_{0.2}Yb)_{0.22}ZrO_{27}$ (HE- RE_2ZrO_{27}) via an electrospinning and annealing process and systematically investigated its microstructure and thermal stability. Figure 9B shows the typical nanofibers and their compositional energy

spectra of HE- $\text{RE}_2\text{ZrO}_{27}$ nanofibers when sintered without insulation at 1000 °C. It can be seen that HE- $\text{RE}_2\text{ZrO}_{27}$ nanofibers are internally composed of fine nanoparticles and various rare-earth elements are uniformly distributed in the fibers, and this structure makes them promising for applications in the field of thermal insulation. Zhu et al. [80] in situ synthesized FeCoNiIrRu HEA nanocrystals in carbon nanofibers (CNFs) using a combination of electrospinning and graphitization and investigated the chemical composition and electronic states of FeCoNiIrRu/CNFs via x-ray photoelectron spectroscopy (Figure 9C).

2.2.6. Spray Pyrolysis

In the spray pyrolysis method, liquid droplet aerosols produced by solution atomization are carried by a carrier gas into a high-temperature reaction furnace. When the water evaporates, the droplets precipitate out of the solid phase due to supersaturation and are transformed into hybridized spherical particles composed of various metal salt elements. Alternatively, the solution is sprayed into a high-temperature atmosphere and dried, followed by a heat treatment to form a powder. The size of the particles formed is highly dependent on the spraying process parameters. The spray method requires high temperature and vacuum conditions and has high requirements in terms of its equipment and operation, but it is easy to produce powders with small particle sizes and good dispersion.

Here, Qiao et al. [81] reported the synthesis of high-entropy phosphate (HEPi) catalysts (CoFeNiMnMoPi) in the form of highly homogeneous spherical particles. As shown in Figure 10a, the metal salt precursors were dissolved in ethanol solution and tri-n-octylphosphine oxide (TOPO) was added. Aerosol droplets were formed by spraying, and the oxide was converted into phosphate in situ during high temperature and rapid heating. Jennifer et al. [82] analyzed the formation mechanism of HEA nanocrystalline-based macro- and mesoporous materials and the role of templating agents by using different templating agents to synthesize HEA via spray pyrolysis. The level of chemical and structural complexity achievable by spray pyrolysis was significantly improved by fabricating HEA-based particles with controlled porosity.

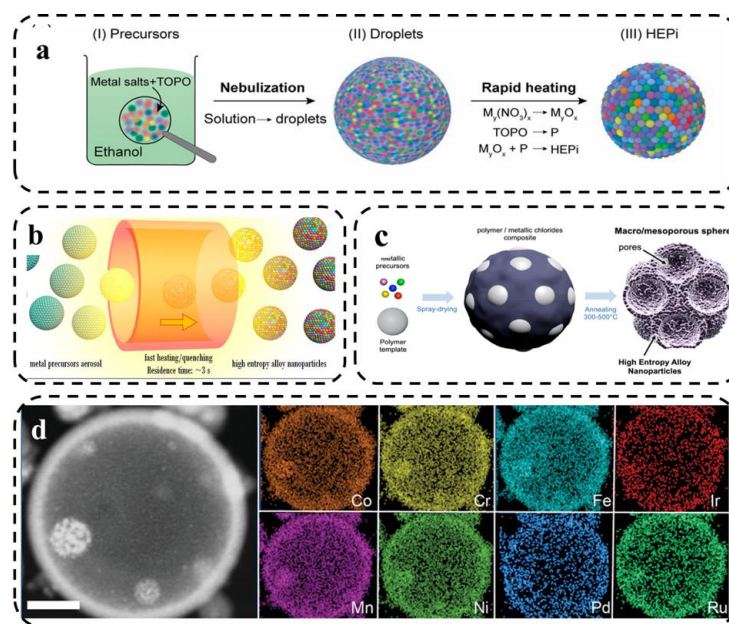


Figure 10. (a) Schematic illustration of the HEPi particle formation process [81]. (b) Schematic of the evolution of aerosol droplets during the high-temperature treatment [73]. (c) Scheme of the fabrication process of porous HEA-based particles by aerosol synthesis followed by thermal annealing [82]. (d) HAADF-STEM image and HAADF-EDS elemental maps of an individual octonary CrMnFeCoNiPdRuIr hollow HEA nanoparticle. Scale bar: 100 nm [83].

2.2.7. Microwave-Assisted Synthesis

Conventional methods for synthesizing HEMs require high temperatures, at ~ 1000 °C. The relatively slow ramp-up rate greatly limits the preparation of HEMs on a large scale. Microwave heating is an effective method for inducing thermal energy and has been used for the synthesis of organic [84] and high-quality carbon materials [85], as well as carbon-loaded nanomaterials [86,87]. This microwave heating method has several advantages: (1) fast heating and cooling rates; (2) high, achievable temperatures; and (3) applicability to carbon materials of various sizes. In view of these advantages, this microwave radiation-induced heating method has great potential to be applied in a wide range of production applications of nanomaterials.

Hu et al. [88] reported a facile, efficient, and scalable microwave heating method for the synthesis of HEA-NPs on carbon-based substrates of different sizes (Figure 11A). They synthesized PtPdFeCoNi HEA-NPs with an average particle size of about 12 nm. Otherwise, there was uniform distribution of various elements owing to decomposition and liquid metal solidification being almost simultaneous without diffusion and phase segregation. In addition to two-dimensional carbon materials such as graphene oxide, this microwave synthesis method can be applied to other carbon-based materials, including one-dimensional materials (e.g., CNFs) and three-dimensional materials (e.g., c-wood), which also have dimensional effects on the particle size of the generated HEA-NPs.

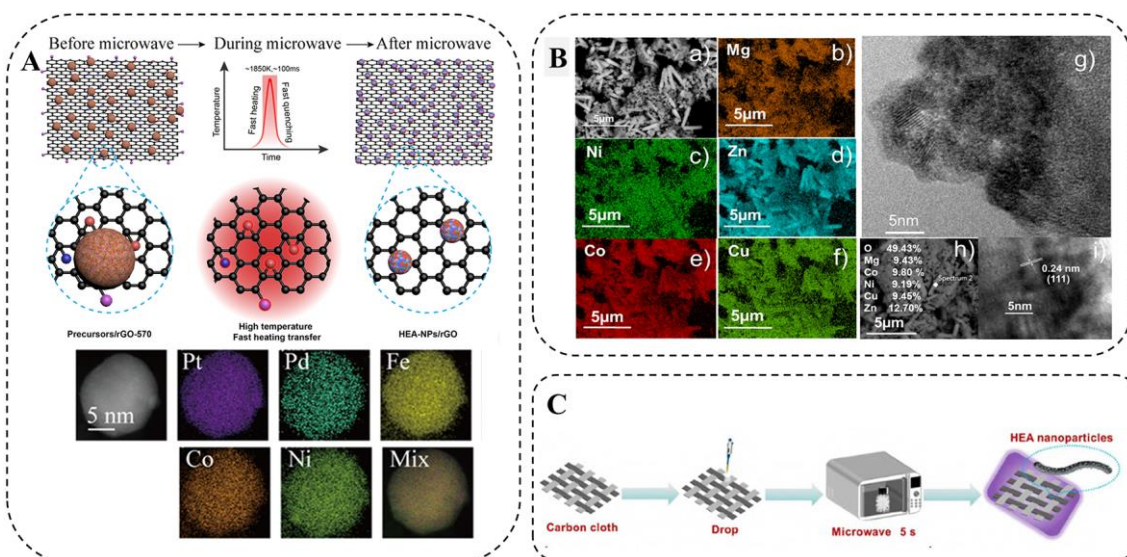


Figure 11. (A) Schematic illustration of the formation of HEA-NPs on rGO by microwave heating, HAADF-STEM image, and STEM-EDS elemental mapping of a PtPdFeCoNi HEA-NPs [88]. (B) SEM image and EDS elemental mapping of (CoCuMgNiZn)O powder [89]. (C) Schematic diagram of microwave-assisted synthesis [90].

Colombo et al. [89] proposed a novel and simple method for the synthesis of HEO materials through microwave radiation. It is worth noting that the five elements are evenly distributed (Figure 11B). Mehdi [90] synthesized HEO (Mg, Cu, Ni, Co, Zn)O nanoparticles through microwave irradiation. In Figure 11C, the preparation process and principles of the material are clearly demonstrated. This method greatly reduces the time and cost of synthesizing HEMs. Microwave-assisted synthesis is also safer than flame pyrolysis [47] and has higher product reproducibility [90].

2.2.8. Pulse Discharge Method

Due to the transient high current density, pulsed electrolysis can increase the cathodic overpotential at the same current density (compared with direct current (DC)). Lu et al. [91] developed a pulsed current electrodeposition method to grow a FeCoNiMnW HEA(H-

FeCoNiMnW) on the surface of carbon paper. As shown in Figure 12a–c, the morphological characterization shows that the material is spherical and has a uniform distribution of various elements, which can be used as an efficient and stable bifunctional electrocatalyst for HER and OER in acidic media.

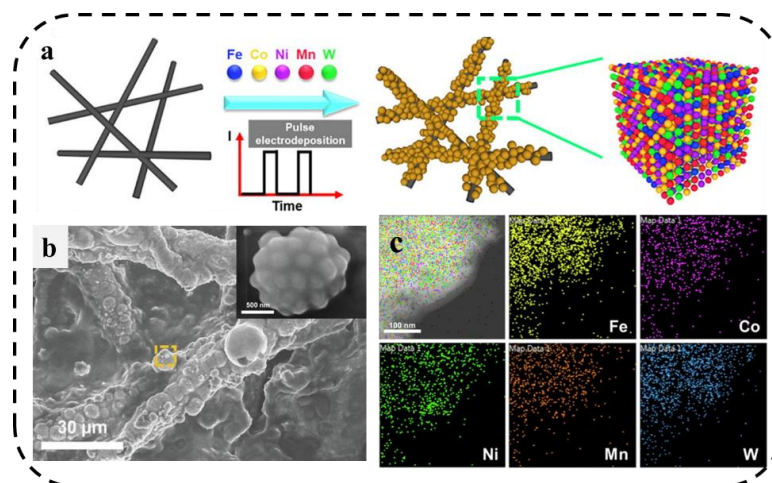


Figure 12. (a) Schematic diagram of preparation of H-FeCoNiMnW. (b) SEM image of H-FeCoNiMnW deposited on carbon paper. (c) TEM/EDX element mapping of H-FeCoNiMnW [91].

3. Application in Lithium–Sulfur Batteries

At present, the development of LSBs urgently needs to be driven by advanced catalytic materials. The surface of HEA is highly heterogeneous due to the mixture of multiple metals, which provides diverse sites for LiPSs to be adsorbed on and reacted with. The activation of multisite HEA electrocatalysts helps to improve the atomic utilization of each metal in polysulfide adsorption [92]. In addition, HEA nanocrystals exhibit highly exposed active surfaces and excellent dynamic structural stability [93]. Multipoint HEA nanocrystal electrocatalysts have become a rising star in recent years due to their flexible elemental composition and customizable electronic structure, providing opportunities for efficient synergistic catalytic polysulfide conversion. This work compares the electrochemical performance of several HEMs applied to LSBs in terms of rate performance (Figure 13a).

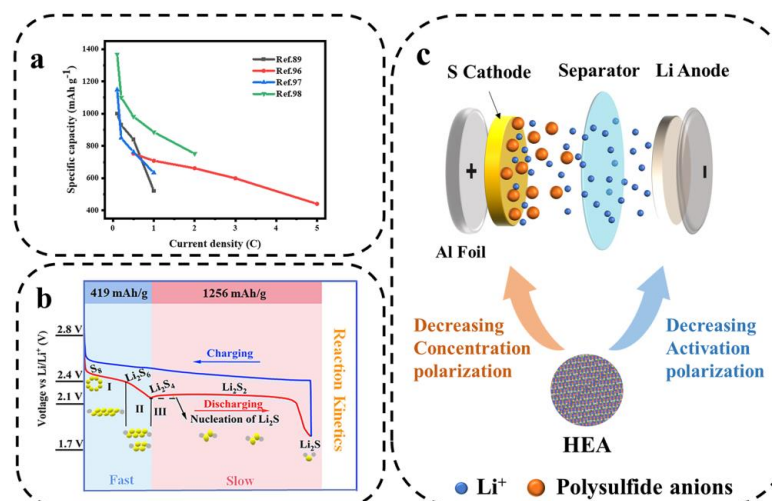


Figure 13. (a) The rate performance of several HEMs used in LSBs. (b) The charging–discharging voltage plateaus of the cathode and the corresponding products in LSBs [94]. (c) Schematic diagram of high-entropy catalysts to reduce the polarization of LSBs.

The reaction process in LSBs involves a series of multi-electron and multi-phase transitions [95]. S₈ active cathode involves a 16-electron transfer reaction ($S_8 + 16 Li^+ + 16e^- \rightleftharpoons 8 Li_2S$), enabling LSBs to achieve a high theoretical capacity of 1675 mAh g⁻¹. In general, LSBs exhibit two discharge voltage plateaus in the capacity–voltage diagram (Figure 13b). During the discharge process, S₈ will first be reduced to a series of intermediate products of long-chain LiPSs (Li_2S_x , $4 \leq x \leq 8$), forming the first upper voltage plateau (~2.3 V). In a continuous lithiation process, soluble long-chain LiPSs are converted to solid-phase short-chain LiPS species Li_2S_2 . Then, Li_2S_2 is converted to Li_2S , providing the second discharge voltage plateau at ~2.1 V. The opposite reactions occur during the charging process. Typically, three types of polarization occur within the cell: activation polarization, concentration polarization, and ohmic polarization. The activation polarization and the concentration polarization can be reduced by changing the composition and structure of the electrode or electrolyte, while ohmic polarization is usually considered an inherent property. As shown in Figure 13c, to reduce polarization and energy loss, catalysts such as HEA can be used to increase the activity of LiPSs around the anode (reducing the concentration polarization) and to accelerate the subsequent redox reaction (reducing the activation polarization) [28].

Xu et al. [28] investigated a nano-HEA composed of five elements, Fe, Co, Ni, Mn, and Zn, as a catalyst for the redox process of LiPSs. As shown in Figure 14a, the metal organic framework-74 (MOF-74) precursor was subjected to rapid CTS reduction to obtain single-phase HEA-NPs, about 7 nm, uniformly distributed on the porous carbon matrix. The test results showed that the capacity retention of LSBs assembled with a nano-HEA modified separator was 83.3% (500 cycles at 2 C rate). Due to the strong affinity of nano-HEA with LiPSs, the activity of adsorbed LiPSs around the electrodes was more than 17 times higher than that of the control sample (without the addition of nano-HEA), which significantly reduced the concentration polarization (Figure 14b).

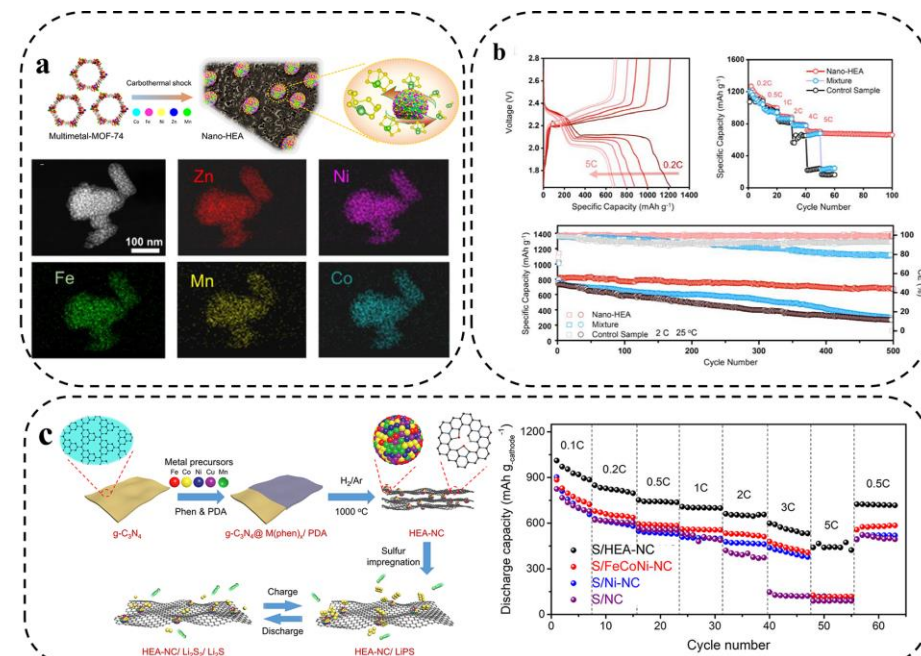


Figure 14. (a) Preparation schematic diagram, morphological characterization, and (b) electrochemical performance of assembled LSBs [28]. (c) Schematic illustration of the preparation of HEA-NC and acceleration for the conversion between LiPSs and Li_2S_2/Li_2S on HEA-NC catalytic host and rate capability [96].

Wang et al. [96] synthesized $Fe_{0.24}Co_{0.26}Ni_{0.10}Cu_{0.15}Mn_{0.25}$ HEA as core catalytic hosts to activate the electrochemical performance of S cathode in LSBs. To further exploit the

advantages of HEA in catalysis, $\text{Fe}_{0.24}\text{Co}_{0.26}\text{Ni}_{0.10}\text{Cu}_{0.15}\text{Mn}_{0.25}$ high-entropy nanocrystals distributed on nitrogen-doped carbon (NC) with good electrical conductivity and affinity for LiPSs were prepared (Figure 14c). As expected, the prepared S/HEA-NC cathode was used to assemble LSBs with excellent rate performance.

Zheng et al. [97] prepared a typical cubic rock salt HEO containing Ni, Mg, Cu, Zn, and Co elements for LSB application via the mechanical ball-milling method combined with a 1000 °C heat treatment (Figure 15A). The high dispersion of metal species in HEMO-1 favors the exposure of active sites, which undoubtedly facilitates the limitation of LiPSs during charge and discharge. Both platforms of HEMO-1 cells are prolonged compared with KB/S cells, indicating the promotion of LiPS conversion. The irregular shape of the prepared HEO volume and the low surface activity may not be conducive to loading sulfur efficiently. In view of these issues, the future development of HEO materials with regular nanostructures is necessary.

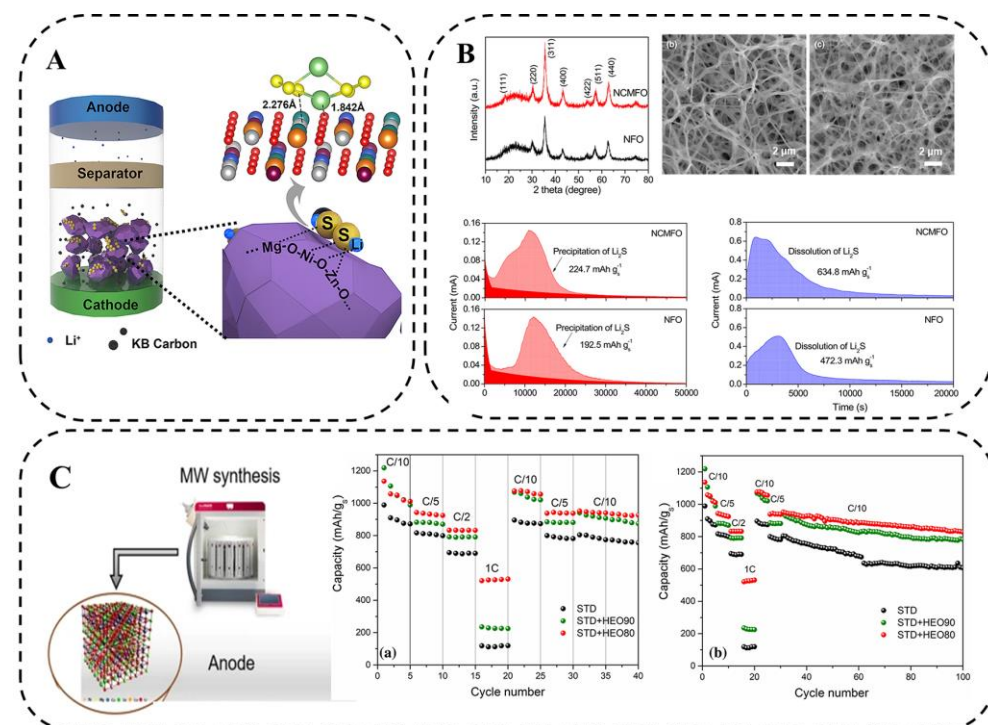


Figure 15. (A) Schematic illustration of cell configuration using HEMO-1 as chemical anchor of polysulfide in cathode for enhancing performance of LSBs. Geometry configuration of Li_2S_6 binding to HEMO-1. (The oxygen, nickel, magnesium, zinc, copper, cobalt, lithium, and sulfur atoms are marked with red, white, orange, green, blue, purple, luminous yellow, and light green, respectively; 2.276 Å and 1.842 Å are simulative bond distances of S-Ni and Li-O, respectively) [97]. (B) XRD pattern, SEM images, Potentiostatic discharge profile at 2.05 V, and potentiostatic charge profile at 2.4 V [98]. (C) Schematic diagram of microwave-assisted hydrothermal synthesis and electrochemical performance [89].

HEO nanofibers ($\text{Mg}_{0.2}\text{Mn}_{0.2}\text{Co}_{0.2}\text{Ni}_{0.2}\text{Zn}_{0.2}\text{Fe}_2\text{O}_4$) were prepared by electrospinning method using a mixture of polyacrylonitrile (PAN) and metal salts by Tian et al. [98]. They applied the HEO nanofibers as catalytic hosts for sulfur in LSBs to promote the conversion of soluble LiPSs. The porous one-dimensional nanostructures synergistically interacted with multiple metal cations in a single spinel structure, which not only provided an ideal pathway to promote Li^+ diffusion but also provided abundant active sites for chemically anchored LiPS and catalytic LiPS conversion. The larger capacity contribution of Li_2S precipitation compared with NiFe_2O_4 (NFO) indicates that $(\text{Ni}_{1/3}\text{Co}_{1/3}\text{Mn}_{1/3})\text{Fe}_2\text{O}_4$ is

more effective in promoting Li_2S nucleation, as well as Li_2S dissolution (Figure 15B). The results show that the S/HEO composites can achieve fast kinetics and good cycling stability.

Colombo et al. [89] designed and synthesized HEO materials ($(\text{CoCuMgNiZn})\text{O}$) via microwave radiation (Figure 15C). Overall, the electrochemical stability of the material and the uniformity and consistency of the composition during charge and discharge ensure efficient and stable operation of the LSBs with a coulombic efficiency of 98.7% over 500 cycles of 0.2 C. Therefore, these low-cost and simple HEO/S cathode preparation techniques can build better and cheaper LSBs and open up new avenues for the application of HEMs in energy conversion and storage devices.

In conclusion, we summarize the application of HEMs for LSBs. Like other modified materials, HEMs are mainly applied to sulfur cathode and separator modification. Like many other electrocatalytic reactions, the conversion of LiPSs in LSBs involves a series of complex multielectron and multiphase conversion processes. The synergistic effect of multiple atoms and sulfur–metal (S–M) chemical interactions between LiPS and HEM hosts significantly affects the electrocatalytic activity of HEMs.

4. Conclusions and Perspectives

LSBs are currently only in the basic research stage and have not been commercialized, which is mainly affected by the insulation of sulfur/lithium sulfide (S/ Li_2S), the fatal shuttle effect of LiPSs, and volume expansion effect [99]. The tunable atomic species of HEMs and the highly heterogeneous of atomic surfaces provides diverse active sites to adsorb and react with LiPSs. The use of HEM electrocatalysts is deemed to be an effective key to inhibiting the shuttle effect and accelerating sulfur reaction kinetics. The well-defined design principle and extensive catalytic mechanism explorations with respect to HEMs have provided valuable guidelines on the construction of high-efficiency and long-lifespan LSBs. Nevertheless, there are still many spaces for persistent explorations in HEM promoters.

(a) The HEMs with high electrocatalytic activity need to be further evolved. A large number of research results have been achieved in the preparation process and tissue properties of HEMs with different compositions, while the compositions of HEMs are complex and variable. The structure–properties relationship of HEMs is still not perfect. Conventional preparation methods require harsh conditions and high temperatures to overcome the reaction energy barrier, making it hard to precisely control the structure of catalytic materials or to produce nanomaterials with large sizes unsuitable for catalysis. Currently, finding a low-temperature method to precisely prepare high-entropy nanomaterials with controllable structure and composition is a difficult problem in the field of HEMs. A breakthrough in the difficulty of preparing HEMs will contribute to carrying out the next step of catalytic performance research. It is expected that HEMs will shine in the field of electrochemical energy storage, represented by LSBs.

(b) The electrocatalytic mechanism of HEMs needs to be deeply revealed. A clear electrocatalytic mechanism understanding is beneficial to constructing HEMs with high electrocatalytic activity. The synergistic interaction (e.g., metallic bond, d-p orbital hybridization, electron spin states, Jahn–Teller effect, and Mott–Schottky heterostructures) largely influences the surface state and the distribution of active sites in HEMs [100]. In addition, metal–sulfur bonding also seriously affects the adsorption of HEMs with polysulfides. It is significant to find out the different bonding mechanisms, which helps to understand the catalytic mechanism of HEMs applied to LSBs and to design specific HEMs.

(c) Advanced in situ characterization techniques need to be extensively developed [101]. The shuttle problem is one of the most important reactions in LSBs. However, the essential catalysts to overcome its sluggish reaction kinetics always undergo a complex dynamic evolution in the actual catalytic process, and the concomitant intermediates and catalytic products also continuously convert and reconstruct. This makes accurately capturing them difficult, making the elucidation of catalytic mechanisms difficult. Thus, it is necessary to use extensive in situ characterization techniques such as XRD, X-ray absorption (XAS), and

Raman spectroscopies to promote real-time reactions during the charging and discharging of LSBs [102].

In total, the use of HEM promoters indeed serves as an effective strategy to optimize the electrochemical reaction approach and to design high-energy density and long-lifespan LSBs. However, a multitude of challenges with regard to advanced Li–S system construction is still expected to be addressed, with persistent efforts from both experimental and theoretical explorations. Real applications of LSBs are expected to be further promoted by active HEM electrocatalysts. Actual application atmospheres, pertaining to high sulfur loading, lean electrolyte usage, and flexibility, cause relatively intricate sulfur reaction processes, leading to the inferior electrochemical performances of LSBs. High-performance LSB systems in future commercial applications might be realized by applying active HEM electrocatalysts.

Author Contributions: Y.Y.: Conceptualization, Methodology, Writing—original draft, Writing—review and editing. J.C.: Literature search, Data analysis, Writing—review and editing, Drawing of figures. R.N.: Literature search, Data collection, Writing—review and editing, Drawing of figures. Z.Z.: Validation, Methodology, Review, Formal analysis. X.W.: Resources, Conceptualization, Validation, Writing—review and editing, Visualization. All authors have read and agreed to the published version of the manuscript.

Funding: The authors appreciate the support from the National Natural Science Foundation of China (grant No. 52072256), the Key R & D program of Shanxi Province (202102030201006), and the Shanxi Science and Technology Major Project (grant No. 20201101016 and 20181102019).

Data Availability Statement: Data are contained within the article.

Conflicts of Interest: The authors declare no conflict of interest.

References

1. Li, H.; Di, S.; Niu, P.; Wang, S.; Wang, J.; Li, L. A durable half-metallic diatomic catalyst for efficient oxygen reduction. *Energy Environ. Sci.* **2022**, *15*, 1601–1610. [[CrossRef](#)]
2. Liu, C.; Xu, D.; Weng, J.; Zhou, S.; Li, W.; Wan, Y.; Jiang, S.; Zhou, D.; Wang, J.; Huang, Q. Phase Change Materials Application in Battery Thermal Management System: A Review. *Materials* **2020**, *13*, 4622. [[CrossRef](#)] [[PubMed](#)]
3. Xu, D.; Huang, G.; Guo, L.; Chen, Y.; Ding, C.; Liu, C. Enhancement of catalytic combustion and thermolysis for treating polyethylene plastic waste. *Adv. Compos. Hybrid Mater.* **2022**, *5*, 113–129. [[CrossRef](#)]
4. Qin, J.; Liu, C.; Huang, Q. Simulation on fire emergency evacuation in special subway station based on Pathfinder. *Case Stud. Therm. Eng.* **2020**, *21*, 100677. [[CrossRef](#)]
5. Yao, X.; Guo, C.; Song, C.; Lu, M.; Zhang, Y.; Zhou, J.; Ding, H.-M.; Chen, Y.; Li, S.-L.; Lan, Y.-Q. In Situ Interweaved High Sulfur Loading Li–S Cathode by Catalytically Active Metalloporphyrin Based Organic Polymer Binders. *Adv. Mater.* **2023**, *35*, 2208846. [[CrossRef](#)] [[PubMed](#)]
6. Zhao, Z.; Yi, Z.; Li, H.; Pathak, R.; Cheng, X.; Zhou, J.; Wang, X.; Qiao, Q. Understanding the modulation effect and surface chemistry in a heteroatom incorporated graphene-like matrix toward high-rate lithium-sulfur batteries. *Nanoscale* **2021**, *13*, 14777–14784. [[CrossRef](#)] [[PubMed](#)]
7. Chen, Y.; Wang, T.; Tian, H.; Su, D.; Zhang, Q.; Wang, G. Advances in Lithium-Sulfur Batteries: From Academic Research to Commercial Viability. *Adv. Mater.* **2021**, *33*, e2003666. [[CrossRef](#)]
8. Ma, J.; Yu, M.; Zhu, J.; Li, W.; Gong, W.; Qiu, H. Enhanced anchoring and catalytic conversion of polysulfides by iron phthalocyanine for graphene-based Li–S batteries. *Ionics* **2021**, *27*, 3007–3016. [[CrossRef](#)]
9. Pang, Y.; Liu, Z.; Shang, C. The construction of quasi-solid state electrolyte with introduction of $\text{Li}_{6.4}\text{La}_3\text{Zr}_{1.4}\text{Ta}_{0.6}\text{O}_{12}$ to suppress lithium polysulfides' shuttle effect in Li–S batteries. *Mater. Lett.* **2023**, *336*, 133874. [[CrossRef](#)]
10. Di, S.; Chen, S.; Chang, C.; Wang, S.; Choi, J.; Li, L. Enhancement of polysulfide trapping induced by faceted ferroelectric for high-performance Li–S batteries. *Scr. Mater.* **2023**, *226*, 115218. [[CrossRef](#)]
11. Zhao, Z.; Pathak, R.; Wang, X.; Yang, Z.; Li, H.; Qiao, Q. Sulfophilic FeP/rGO as a highly efficient sulfur host for propelling redox kinetics toward stable lithium-sulfur battery. *Electrochim. Acta* **2020**, *364*, 137117. [[CrossRef](#)]
12. Xie, F.; Xu, C.; Song, Y.; Liang, Q.; Ji, J.; Wang, S. 2D–2D heterostructure of ionic liquid-exfoliated MoS₂/MXene as lithium polysulfide barrier for Li–S batteries. *J. Colloid Interface Sci.* **2023**, *636*, 528–536. [[CrossRef](#)]
13. Liu, C.; Huang, Q.; Zheng, K.; Qin, J.; Zhou, D.; Wang, J. Impact of Lithium Salts on the Combustion Characteristics of Electrolyte under Diverse Pressures. *Energies* **2020**, *13*, 5373. [[CrossRef](#)]
14. Yao, Y.; Zhao, Z.; Ren, R.; Wang, X. Tailoring nickel–cobalt bimetallic alloy as highly effective catalyst in modified separators for high-performance lithium-sulfur batteries. *J. Alloys Compd.* **2023**, *945*, 169242. [[CrossRef](#)]

15. Deng, N.; Peng, Z.; Tian, X.; Li, Y.; Yan, J.; Liu, Y.; Kang, W. Yttrium trifluoride doped polyacrylonitrile based carbon nanofibers as separator coating layer for high performance lithium-metal batteries. *J. Colloid Interface Sci.* **2023**, *634*, 949–962. [[CrossRef](#)]
16. Wang, W.; Wang, X.; Shan, J.; Yue, L.; Wang, W.; Li, Y. Conductive few-layered 1T-MoSe₂/MXene as a highly-efficient catalyst for accelerating bidirectional sulfur redox kinetics in Li-S batteries. *J. Alloys Compd.* **2023**, *936*, 168250. [[CrossRef](#)]
17. Zhao, Z.; Duan, Y.; Chen, F.; Tian, Z.; Pathak, R.; Elam, J.W.; Yi, Z.; Wang, Y.; Wang, X. Multifunctional transitional metal-based phosphide nanoparticles towards improved polysulfide confinement and redox kinetics for highly stable lithium-sulfur batteries. *Chem. Eng. J.* **2022**, *450*, 138310. [[CrossRef](#)]
18. Hua, W.; Xia, J.; Hu, Z.; Li, H.; Lv, W.; Yang, Q.-H. Bimetallic Compound Catalysts with Multiple Active Centers for Accelerated Polysulfide Conversion in Li-S Batteries. *J. Electrochem.* **2022**. [[CrossRef](#)]
19. Huang, Y.; Lin, L.; Zhang, C.; Liu, L.; Li, Y.; Qiao, Z.; Lin, J.; Wei, Q.; Wang, L.; Xie, Q.; et al. Recent Advances and Strategies toward Polysulfides Shuttle Inhibition for High-Performance Li-S Batteries. *Adv. Sci.* **2022**, *9*, e2106004. [[CrossRef](#)]
20. Xiao, R.; Luo, D.; Wang, J.; Lu, H.; Ma, H.; Akinoglu, E.M.; Jin, M.; Wang, X.; Zhang, Y.; Chen, Z. Oxidation States Regulation of Cobalt Active Sites through Crystal Surface Engineering for Enhanced Polysulfide Conversion in Lithium–Sulfur Batteries. *Adv. Sci.* **2022**, *9*, 2202352. [[CrossRef](#)]
21. Ren, R.; Zhao, Z.; Meng, Z.; Wang, X. Hollow heterostructure design enables self-cleaning surface for enhanced polysulfides conversion in advanced lithium-sulfur batteries. *J. Colloid Interface Sci.* **2022**, *608*, 1576–1584. [[CrossRef](#)] [[PubMed](#)]
22. Wu, Z.-P.; Caracciolo, D.T.; Maswadeh, Y.; Wen, J.; Kong, Z.; Shan, S.; Vargas, J.A.; Yan, S.; Hopkins, E.; Park, K.; et al. Alloying–realloying enabled high durability for Pt-Pd-3d-transition metal nanoparticle fuel cell catalysts. *Nat. Commun.* **2021**, *12*, 859. [[CrossRef](#)]
23. Li, T.; Yao, Y.; Huang, Z.; Xie, P.; Liu, Z.; Yang, M.; Gao, J.; Zeng, K.; Brozena, A.H.; Pastel, G.; et al. Denary oxide nanoparticles as highly stable catalysts for methane combustion. *Nat. Catal.* **2021**, *4*, 62–70. [[CrossRef](#)]
24. Liang, W.; Wang, Y.; Zhao, L.; Guo, W.; Li, D.; Qin, W.; Wu, H.; Sun, Y.; Jiang, L. 3D Anisotropic Au@Pt–Pd Hemispherical Nanostructures as Efficient Electrocatalysts for Methanol, Ethanol, and Formic Acid Oxidation Reaction. *Adv. Mater.* **2021**, *33*, 2100713. [[CrossRef](#)] [[PubMed](#)]
25. Koo, W.-T.; Millstone, J.E.; Weiss, P.S.; Kim, I.-D. The Design and Science of Polyelemental Nanoparticles. *ACS Nano* **2020**, *14*, 6407–6413. [[CrossRef](#)] [[PubMed](#)]
26. Yeh, J.-W.; Chen, S.-K.; Lin, S.-J.; Gan, J.-Y.; Chin, T.-S.; Shun, T.-T.; Tsau, C.-H.; Chang, S.-Y. Nanostructured High-Entropy Alloys with Multiple Principal Elements: Novel Alloy Design Concepts and Outcomes. *Adv. Eng. Mater.* **2004**, *6*, 299–303. [[CrossRef](#)]
27. Cantor, B.; Chang, I.T.H.; Knight, P.; Vincent, A.J.B. Microstructural development in equiatomic multicomponent alloys. *Mater. Sci. Eng. A* **2004**, *375*–377, 213–218. [[CrossRef](#)]
28. Xu, H.; Hu, R.; Zhang, Y.; Yan, H.; Zhu, Q.; Shang, J.; Yang, S.; Li, B. Nano high-entropy alloy with strong affinity driving fast polysulfide conversion towards stable lithium sulfur batteries. *Energy Storage Mater.* **2021**, *43*, 212–220. [[CrossRef](#)]
29. Tsai, M.-H.; Yeh, J.-W. High-Entropy Alloys: A Critical Review. *Mater. Res. Lett.* **2014**, *2*, 107–123. [[CrossRef](#)]
30. Xin, Y.; Li, S.; Qian, Y.; Zhu, W.; Yuan, H.; Jiang, P.; Guo, R.; Wang, L. High-Entropy Alloys as a Platform for Catalysis: Progress, Challenges, and Opportunities. *ACS Catal.* **2020**, *10*, 11280–11306. [[CrossRef](#)]
31. Wang, B.; Wang, C.; Yu, X.; Cao, Y.; Gao, L.; Wu, C.; Yao, Y.; Lin, Z.; Zou, Z. General synthesis of high-entropy alloy and ceramic nanoparticles in nanoseconds. *Nat. Synth.* **2022**, *1*, 138–146. [[CrossRef](#)]
32. Lei, Z.; Liu, X.; Wang, H.; Wu, Y.; Jiang, S.; Lu, Z. Development of advanced materials via entropy engineering. *Scr. Mater.* **2019**, *165*, 164–169. [[CrossRef](#)]
33. Liu, J.; Li, Y.; Chen, Z.; Liu, N.; Zheng, L.; Shi, W.; Wang, X. Polyoxometalate Cluster-Incorporated High Entropy Oxide Sub-1 nm Nanowires. *J. Am. Chem. Soc.* **2022**, *144*, 23191–23197. [[CrossRef](#)]
34. Oses, C.; Toher, C.; Curtarolo, S. High-entropy ceramics. *Nat. Rev. Mater.* **2020**, *5*, 295–309. [[CrossRef](#)]
35. Xiang, H.; Xing, Y.; Dai, F.; Wang, H.; Su, L.; Miao, L.; Zhang, G.; Wang, Y.; Qi, X.; Yao, L.; et al. High-entropy ceramics: Present status, challenges, and a look forward. *J. Adv. Ceram.* **2021**, *10*, 385–441. [[CrossRef](#)]
36. Yao, Y.; Liu, Z.; Xie, P.; Huang, Z.; Li, T.; Morris, D.; Finfrock, Z.; Zhou, J.; Jiao, M.; Gao, J.; et al. Computationally aided, entropy-driven synthesis of highly efficient and durable multi-elemental alloy catalysts. *Sci. Adv.* **2020**, *6*, eaaz0510. [[CrossRef](#)]
37. Liu, M.; Zhang, Z.; Okejiri, F.; Yang, S.; Zhou, S.; Dai, S. Entropy-Maximized Synthesis of Multimetallic Nanoparticle Catalysts via a Ultrasonication-Assisted Wet Chemistry Method under Ambient Conditions. *Adv. Mater. Interfaces* **2019**, *6*, 1900015. [[CrossRef](#)]
38. Nandan, R.; Raj, G.; Nanda, K.K. FeCoNiMnCr High-Entropy Alloy Nanoparticle-Grafted NCNTs with Promising Performance in the Ohmic Polarization Region of Fuel Cells. *ACS Appl. Mater. Interfaces* **2022**, *14*, 16108–16116. [[CrossRef](#)] [[PubMed](#)]
39. Zhao, P.; Cao, Q.; Yi, W.; Hao, X.; Li, J.; Zhang, B.; Huang, L.; Huang, Y.; Jiang, Y.; Xu, B.; et al. Facile and General Method to Synthesize Pt-Based High-Entropy-Alloy Nanoparticles. *ACS Nano* **2022**, *16*, 14017–14028. [[CrossRef](#)]
40. Zhan, C.; Bu, L.; Sun, H.; Huang, X.; Zhu, Z.; Yang, T.; Ma, H.; Li, L.; Wang, Y.; Geng, H.; et al. Medium/High-Entropy Amalgamated Core/Shell Nanoplate Achieves Efficient Formic Acid Catalysis for Direct Formic Acid Fuel Cell. *Angew. Chem. Int. Ed. Engl.* **2023**, *62*, e202213783. [[CrossRef](#)] [[PubMed](#)]
41. Qiu, H.-J.; Fang, G.; Wen, Y.; Liu, P.; Xie, G.; Liu, X.; Sun, S. Nanoporous high-entropy alloys for highly stable and efficient catalysts. *J. Mater. Chem. A* **2019**, *7*, 6499–6506. [[CrossRef](#)]

42. Yusenko, K.V.; Riva, S.; Carvalho, P.A.; Yusenko, M.V.; Arnaboldi, S.; Sukhikh, A.S.; Hanfland, M.; Gromilov, S.A. First hexagonal close packed high-entropy alloy with outstanding stability under extreme conditions and electrocatalytic activity for methanol oxidation. *Scr. Mater.* **2017**, *138*, 22–27. [[CrossRef](#)]
43. Liu, X.; Duan, Y.; Guo, Y.; Pang, H.; Li, Z.; Sun, X.; Wang, T. Microstructure Design of High-Entropy Alloys Through a Multistage Mechanical Alloying Strategy for Temperature-Stable Megahertz Electromagnetic Absorption. *Nano-Micro Lett.* **2022**, *14*, 142. [[CrossRef](#)] [[PubMed](#)]
44. Akrami, S.; Edalati, P.; Fuji, M.; Edalati, K. High-entropy ceramics: Review of principles, production and applications. *Mater. Sci. Eng. R Rep.* **2021**, *146*, 100644. [[CrossRef](#)]
45. Pedersen, J.K.; Batchelor, T.A.A.; Bagger, A.; Rossmeisl, J. High-Entropy Alloys as Catalysts for the CO₂ and CO Reduction Reactions. *ACS Catal.* **2020**, *10*, 2169–2176. [[CrossRef](#)]
46. Batchelor, T.A.A.; Pedersen, J.K.; Winther, S.H.; Castelli, I.E.; Jacobsen, K.W.; Rossmeisl, J. High-Entropy Alloys as a Discovery Platform for Electrocatalysis. *Joule* **2019**, *3*, 834–845. [[CrossRef](#)]
47. Nagy, P.; Rohbeck, N.; Roussely, G.; Sortais, P.; Lábár, J.L.; Gubicza, J.; Michler, J.; Pethö, L. Processing and characterization of a multibeam sputtered nanocrystalline CoCrFeNi high-entropy alloy film. *Surf. Coat. Technol.* **2020**, *386*, 125465. [[CrossRef](#)]
48. Xie, P.; Yao, Y.; Huang, Z.; Liu, Z.; Zhang, J.; Li, T.; Wang, G.; Shahbazian-Yassar, R.; Hu, L.; Wang, C. Highly efficient decomposition of ammonia using high-entropy alloy catalysts. *Nat. Commun.* **2019**, *10*, 4011. [[CrossRef](#)]
49. Xu, K.; Liu, Z.; Yu, H.; Zhong, X.; Zhang, H.; Liu, Z. Improved efficiency for preparing hard magnetic Sm₂Fe₁₇N_X powders by plasma assisted ball milling followed by nitriding. *J. Magn. Magn. Mater.* **2020**, *500*, 166383. [[CrossRef](#)]
50. Shah, D.J.; Sharma, A.S.; Sharma, V.S.; Vishwakarma, V.K.; Sudhakar, A.A.; Shrivastav, P.S.; Varma, R.S. Microcrystalline Cellulose Decorated with Fe₃O₄ Nanoparticle Catalysts for the Microwave-Assisted Synthesis of Thioglyoxamides. *ACS Appl. Nano Mater.* **2023**, *6*, 4005–4016. [[CrossRef](#)]
51. Li, T.; Luo, G.; Liu, K.; Li, X.; Sun, D.; Xu, L.; Li, Y.; Tang, Y. Encapsulation of Ni₃Fe Nanoparticles in N-Doped Carbon Nanotube-Grafted Carbon Nanofibers as High-Efficiency Hydrogen Evolution Electrocatalysts. *Adv. Funct. Mater.* **2018**, *28*, 1805828. [[CrossRef](#)]
52. Lee, W.; Nam, J.; Park, J.; Lee, G.; Ahn, S.H.; Kim, K.S.; Lee, J.-O.; Choi, C.-J.; Hwang, J.Y. Single process of pulsed wire discharge for defect healing and reduction of graphene oxide. *Carbon* **2023**, *201*, 1184–1192. [[CrossRef](#)]
53. Wang, X.; Huang, Z.; Yao, Y.; Qiao, H.; Zhong, G.; Pei, Y.; Zheng, C.; Kline, D.; Xia, Q.; Lin, Z.; et al. Continuous 2000 K droplet-to-particle synthesis. *Mater. Today* **2020**, *35*, 106–114. [[CrossRef](#)]
54. Chen, Y.-W.; Ruan, J.-J.; Ting, J.-M.; Su, Y.-H.; Chang, K.-S. Solution-based fabrication of high-entropy Ba(Ti,Hf,Zr,Fe,Sn)O₃ films on fluorine-doped tin oxide substrates and their piezoelectric responses. *Ceram. Int.* **2021**, *47*, 11451–11458. [[CrossRef](#)]
55. Sarkar, A.; Djenadic, R.; Usharani, N.J.; Sanghvi, K.P.; Chakravadhanula, V.S.K.; Gandhi, A.S.; Hahn, H.; Bhattacharya, S.S. Nanocrystalline multicomponent entropy stabilised transition metal oxides. *J. Eur. Ceram. Soc.* **2017**, *37*, 747–754. [[CrossRef](#)]
56. Dąbrowa, J.; Stygar, M.; Miku, A.; Knapik, A.; Mroczka, K.; Tejchman, W.; Danielewski, M.; Martin, M. Synthesis and microstructure of the (Co,Cr,Fe,Mn,Ni)₃O₄ high entropy oxide characterized by spinel structure. *Mater. Lett.* **2018**, *216*, 32–36. [[CrossRef](#)]
57. Jiang, Q.; Gu, J.; Zhang, L.; Liu, K.; Huang, M.; Liu, P.; Zuo, S.; Wang, Y.; Ma, P.; Fu, Z. A Highly Efficient High-Entropy Metal Hydroxymethylate Electrocatalyst for Oxygen Evolution Reaction. *Chem. Eng. J.* **2022**, *453*, 139510. [[CrossRef](#)]
58. Wu, D.; Kusada, K.; Yamamoto, T.; Toriyama, T.; Matsumura, S.; Kawaguchi, S.; Kubota, Y.; Kitagawa, H. Platinum-Group-Metal High-Entropy-Alloy Nanoparticles. *J. Am. Chem. Soc.* **2020**, *142*, 13833–13838. [[CrossRef](#)]
59. Broge, N.L.N.; Bondesgaard, M.; Søndergaard-Pedersen, F.; Roelsgaard, M.; Iversen, B.B. Autocatalytic Formation of High-Entropy Alloy Nanoparticles. *Angew. Chem.* **2020**, *132*, 22104–22108. [[CrossRef](#)]
60. Grzesik, Z.; Smola, G.; Miszczałk, M.; Stygar, M.; Dąbrowa, J.; Zajusz, M.; Świerczek, K.; Danielewski, M. Defect structure and transport properties of (Co,Cr,Fe,Mn,Ni)₃O₄ spinel-structured high entropy oxide. *J. Eur. Ceram. Soc.* **2020**, *40*, 835–839. [[CrossRef](#)]
61. Vinnik, D.A.; Trofimov, E.A.; Zhivulin, V.E.; Zaitseva, O.V.; Zherebtsov, D.A.; Starikov, A.Y.; Sherstyuk, D.P.; Gudkova, S.A.; Taskaev, S.V. The new extremely substituted high entropy (Ba,Sr,Ca,La)Fe_{6-x}(Al,Ti,Cr,Ga,In,Cu,W)_xO₁₉ microcrystals with magnetoplumbite structure. *Ceram. Int.* **2020**, *46*, 9656–9660. [[CrossRef](#)]
62. Gild, J.; Samicee, M.; Braun, J.L.; Harrington, T.; Vega, H.; Hopkins, P.E.; Vecchio, K.; Luo, J. High-entropy fluorite oxides. *J. Eur. Ceram. Soc.* **2018**, *38*, 3578–3584. [[CrossRef](#)]
63. Rekha, M.Y.; Mallik, N.; Srivastava, C. First Report on High Entropy Alloy Nanoparticle Decorated Graphene. *Sci. Rep.* **2018**, *8*, 8737. [[CrossRef](#)] [[PubMed](#)]
64. Jin, T.; Sang, X.; Unocic, R.R.; Kinch, R.T.; Liu, X.; Hu, J.; Liu, H.; Dai, S. Mechanochemical-Assisted Synthesis of High-Entropy Metal Nitride via a Soft Urea Strategy. *Adv. Mater.* **2018**, *30*, 1707512. [[CrossRef](#)] [[PubMed](#)]
65. Prasad, H.; Singh, S.; Panigrahi, B.B. Mechanical activated synthesis of alumina dispersed FeNiCoCrAlMn high entropy alloy. *J. Alloys Compd.* **2017**, *692*, 720–726. [[CrossRef](#)]
66. Fritze, S.; Koller, C.M.; von Fieandt, L.; Malinovskis, P.; Johansson, K.; Lewin, E.; Mayrhofer, P.H.; Jansson, U. Influence of Deposition Temperature on the Phase Evolution of HfNbTiVZr High-Entropy Thin Films. *Materials* **2019**, *12*, 587. [[CrossRef](#)] [[PubMed](#)]
67. Zhang, Y.; Yan, X.-H.; Liao, W.-B.; Zhao, K. Effects of Nitrogen Content on the Structure and Mechanical Properties of (Al_{0.5}CrFeNiTi_{0.25})Nx High-Entropy Films by Reactive Sputtering. *Entropy* **2018**, *20*, 624. [[CrossRef](#)]

68. Manoj, T.; Perumal, H.P.; Paikaray, B.; Haldar, A.; Sinha, J.; Bhattacharjee, P.P.; Murapaka, C. Perpendicular magnetic anisotropy in a sputter deposited nanocrystalline high entropy alloy thin film. *J. Alloys Compd.* **2023**, *930*, 167337. [\[CrossRef\]](#)
69. He, L.; Liu, C.; Zhao, S.; Shu, C.; Yang, J.; Liu, H.; Zhang, W.; Lin, J.; Long, J.; Chang, H. Microstructure, mechanical and corrosion properties of high hardness TiVZrCrAl HEA coatings prepared by magnetron sputtering. *Surf. Coat. Technol.* **2022**, *441*, 128532. [\[CrossRef\]](#)
70. Löffler, T.; Meyer, H.; Savan, A.; Wilde, P.; Manjón, A.G.; Chen, Y.-T.; Ventosa, E.; Scheu, C.; Ludwig, A.; Schuhmann, W. Discovery of a Multinary Noble Metal-Free Oxygen Reduction Catalyst. *Adv. Energy Mater.* **2018**, *8*, 1802269. [\[CrossRef\]](#)
71. Meyer, H.; Meischein, M.; Ludwig, A. Rapid Assessment of Sputtered Nanoparticle Ionic Liquid Combinations. *ACS Comb. Sci.* **2018**, *20*, 243–250. [\[CrossRef\]](#) [\[PubMed\]](#)
72. Song, J.-Y.; Kim, C.; Kim, M.; Cho, K.M.; Gereige, I.; Jung, W.-B.; Jeong, H.; Jung, H.-T. Generation of High-Density Nanoparticles in the Carbothermal Shock Method. *Sci. Adv.* **2021**, *7*, eabk2984. [\[CrossRef\]](#)
73. Yang, Y.; Song, B.; Ke, X.; Xu, F.; Bozhilov, K.N.; Hu, L.; Shahbazian-Yassar, R.; Zachariah, M.R. Aerosol Synthesis of High Entropy Alloy Nanoparticles. *Langmuir* **2020**, *36*, 1985–1992. [\[CrossRef\]](#) [\[PubMed\]](#)
74. Lacey, S.D.; Dong, Q.; Huang, Z.; Luo, J.; Xie, H.; Lin, Z.; Kirsch, D.J.; Vattipalli, V.; Povinelli, C.; Fan, W.; et al. Stable Multimetallic Nanoparticles for Oxygen Electrocatalysis. *Nano Lett.* **2019**, *19*, 5149–5158. [\[CrossRef\]](#) [\[PubMed\]](#)
75. Wu, Y.; Lei, Z.; Liu, X.; Wang, H.; Lu, Z. Eight in one: High-entropy-alloy nanoparticles synthesized by carbothermal shock. *Sci. Bull.* **2018**, *63*, 737–738. [\[CrossRef\]](#)
76. Yao, Y.; Huang, Z.; Xie, P.; Lacey, S.D.; Jacob, R.J.; Xie, H.; Chen, F.; Nie, A.; Pu, T.; Rehwoldt, M.; et al. Carbothermal shock synthesis of high-entropy-alloy nanoparticles. *Science* **2018**, *359*, 1489–1494. [\[CrossRef\]](#) [\[PubMed\]](#)
77. Wu, H.; Lu, Q.; Li, Y.; Wang, J.; Li, Y.; Jiang, R.; Zhang, J.; Zheng, X.; Han, X.; Zhao, N.; et al. Rapid Joule-Heating Synthesis for Manufacturing High-Entropy Oxides as Efficient Electrocatalysts. *Nano Lett.* **2022**, *22*, 6492–6500. [\[CrossRef\]](#)
78. Xing, Y.; Dan, W.; Fan, Y.; Li, X. Low temperature synthesis of high-entropy $(\text{Y}_{0.2}\text{Yb}_{0.2}\text{Sm}_{0.2}\text{Eu}_{0.2}\text{Er}_{0.2})_2\text{O}_3$ nanofibers by a novel electrospinning method. *J. Mater. Sci. Technol.* **2022**, *103*, 215–220. [\[CrossRef\]](#)
79. Li, Z.; Zhou, F.; Xu, B.; Guo, D. Characterization of novel high-entropy $(\text{La}_{0.2}\text{Nd}_{0.2}\text{Sm}_{0.2}\text{Dy}_{0.2}\text{Yb}_{0.2})_2\text{Zr}_2\text{O}_7$ electrospun ceramic nanofibers. *Ceram. Int.* **2022**, *48*, 12074–12078. [\[CrossRef\]](#)
80. Zhu, H.; Zhu, Z.; Hao, J.; Sun, S.; Lu, S.; Wang, C.; Ma, P.; Dong, W.; Du, M. High-entropy alloy stabilized active Ir for highly efficient acidic oxygen evolution. *Chem. Eng. J.* **2022**, *431*, 133251. [\[CrossRef\]](#)
81. Qiao, H.; Wang, X.; Dong, Q.; Zheng, H.; Chen, G.; Hong, M.; Yang, C.-P.; Wu, M.; He, K.; Hu, L. A high-entropy phosphate catalyst for oxygen evolution reaction. *Nano Energy* **2021**, *86*, 106029. [\[CrossRef\]](#)
82. De Marco, M.L.; Baaziz, W.; Sharna, S.; Devred, F.; Poleunis, C.; Chevillot-Biraud, A.; Nowak, S.; Haddad, R.; Odziomek, M.; Boissière, C.; et al. High-Entropy-Alloy Nanocrystal Based Macro- and Mesoporous Materials. *ACS Nano* **2022**, *16*, 15837–15849. [\[CrossRef\]](#) [\[PubMed\]](#)
83. Wang, X.; Dong, Q.; Qiao, H.; Huang, Z.; Saray, M.T.; Zhong, G.; Lin, Z.; Cui, M.; Brozena, A.; Hong, M.; et al. Continuous Synthesis of Hollow High-Entropy Nanoparticles for Energy and Catalysis Applications. *Adv. Mater.* **2020**, *32*, e2002853. [\[CrossRef\]](#) [\[PubMed\]](#)
84. Kappe, C.O. Controlled Microwave Heating in Modern Organic Synthesis. *Angew. Chem. Int. Ed.* **2004**, *43*, 6250–6284. [\[CrossRef\]](#) [\[PubMed\]](#)
85. Wang, D.; Dai, R.; Zhang, X.; Liu, L.; Zhuang, H.; Lu, Y.; Wang, Y.; Liao, Y.; Nian, Q. Scalable and controlled creation of nanoholes in graphene by microwave-assisted chemical etching for improved electrochemical properties. *Carbon* **2020**, *161*, 880–891. [\[CrossRef\]](#)
86. Tian, Y.; Sarwar, S.; Zheng, Y.; Wang, S.; Guo, Q.; Luo, J.; Zhang, X. Ultrafast microwave manufacturing of MoP/MoO₂/carbon nanotube arrays for high-performance supercapacitors. *J. Solid State Electrochem.* **2020**, *24*, 809–819. [\[CrossRef\]](#)
87. Huang, H.; Zhou, S.; Yu, C.; Huang, H.; Zhao, J.; Dai, L.; Qiu, J. Rapid and energy-efficient microwave pyrolysis for high-yield production of highly-active bifunctional electrocatalysts for water splitting. *Energy Environ. Sci.* **2020**, *13*, 545–553. [\[CrossRef\]](#)
88. Qiao, H.; Saray, M.T.; Wang, X.; Xu, S.; Chen, G.; Huang, Z.; Chen, C.; Zhong, G.; Dong, Q.; Hong, M.; et al. Scalable Synthesis of High Entropy Alloy Nanoparticles by Microwave Heating. *ACS Nano* **2021**, *15*, 14928–14937. [\[CrossRef\]](#)
89. Colombo, R.; Garino, N.; Versaci, D.; Amici, J.; Para, M.L.; Quartarone, E.; Francia, C.; Bella, F.; Bodoardo, S. Designing a double-coated cathode with high entropy oxides by microwave-assisted hydrothermal synthesis for highly stable Li-S batteries. *J. Mater. Sci.* **2022**, *57*, 15690–15704. [\[CrossRef\]](#)
90. Kheradmandfar, M.; Minouei, H.; Tsvetkov, N.; Vayghan, A.K.; Kashani-Bozorg, S.F.; Kim, G.; Hong, S.I.; Kim, D.-E. Ultrafast green microwave-assisted synthesis of high-entropy oxide nanoparticles for Li-ion battery applications. *Mater. Chem. Phys.* **2021**, *262*, 124265. [\[CrossRef\]](#)
91. Chang, S.-Q.; Cheng, C.-C.; Cheng, P.-Y.; Huang, C.-L.; Lu, S.-Y. Pulse electrodeposited FeCoNiMnW high entropy alloys as efficient and stable bifunctional electrocatalysts for acidic water splitting. *Chem. Eng. J.* **2022**, *446*, 137452. [\[CrossRef\]](#)
92. Wang, J.; Zhang, J.; Hu, Y.; Jiang, H.; Li, C. Activating multisite high-entropy alloy nanocrystals via enriching M-pyridinic N-C bonds for superior electrocatalytic hydrogen evolution. *Sci. Bull.* **2022**, *67*, 1890–1897. [\[CrossRef\]](#)
93. Marques, F.; Balcerzak, M.; Winkelmann, F.; Zepon, G. Felderhoff, Review and outlook on high-entropy alloys for hydrogen storage. *Energy Environ. Sci.* **2021**, *14*, 5191–5227. [\[CrossRef\]](#)

94. Wu, J.; Ye, T.; Wang, Y.; Yang, P.; Wang, Q.; Kuang, W.; Chen, X.; Duan, G.; Yu, L.; Jin, Z.; et al. Understanding the Catalytic Kinetics of Polysulfide Redox Reactions on Transition Metal Compounds in Li–S Batteries. *ACS Nano* **2022**, *16*, 15734–15759. [CrossRef] [PubMed]
95. Zhao, Z.; Yi, Z.; Li, H.; Pathak, R.; Yang, Z.; Wang, X.; Qiao, Q. Synergetic effect of spatially separated dual co-catalyst for accelerating multiple conversion reaction in advanced lithium sulfur batteries. *Nano Energy* **2021**, *81*, 105621. [CrossRef]
96. Wang, Z.; Ge, H.; Liu, S.; Li, G.; Gao, X. High-Entropy Alloys to Activate the Sulfur Cathode for Lithium–Sulfur Batteries. *Energy Environ. Mater.* **2022**, *0*, 1–10. [CrossRef]
97. Zheng, Y.; Yi, Y.; Fan, M.; Liu, H.; Li, X.; Zhang, R.; Li, M.; Qiao, Z.-A. A high-entropy metal oxide as chemical anchor of polysulfide for lithium-sulfur batteries. *Energy Storage Mater.* **2019**, *23*, 678–683. [CrossRef]
98. Tian, L.; Zhang, Z.; Liu, S.; Li, G.; Gao, X. High-Entropy Spinel Oxide Nanofibers as Catalytic Sulfur Hosts Promise the High Gravimetric and Volumetric Capacities for Lithium–Sulfur Batteries. *Energy Environ. Mater.* **2022**, *5*, 645–654. [CrossRef]
99. Kang, X.; Jin, Z.; Peng, H.; Cheng, Z.; Liu, L.; Li, X.; Xie, L.; Zhang, J.; Dong, Y. The role of selenium vacancies functionalized mediator of bimetal (Co, Fe) selenide for high-energy-density lithium-sulfur batteries. *J. Colloid Interface Sci.* **2023**, *637*, 161–172. [CrossRef]
100. Zhao, Z.; Yi, Z.; Duan, Y.; Pathak, R.; Cheng, X.; Wang, Y.; Elam, J.W.; Wang, X. Regulating the d-p band center of FeP/Fe₂P heterostructure host with built-in electric field enabled efficient bidirectional electrocatalyst toward advanced lithium-sulfur batteries. *Chem. Eng. J.* **2023**, *463*, 142397. [CrossRef]
101. Zhao, J.; Lian, J.; Zhao, Z.; Wang, X.; Zhang, J. A Review of In-Situ Techniques for Probing Active Sites and Mechanisms of Electrocatalytic Oxygen Reduction Reactions. *Nano-Micro Lett.* **2022**, *15*, 19. [CrossRef] [PubMed]
102. Sturman, J.W.; Baranova, E.A.; Abu-Lebdeh, Y. Review: High-Entropy Materials for Lithium-Ion Battery Electrodes. *Front. Energy Res.* **2022**, *10*. Available online: <https://www.frontiersin.org/articles/10.3389/fenrg.2022.862551> (accessed on 15 March 2023). [CrossRef]

Disclaimer/Publisher’s Note: The statements, opinions and data contained in all publications are solely those of the individual author(s) and contributor(s) and not of MDPI and/or the editor(s). MDPI and/or the editor(s) disclaim responsibility for any injury to people or property resulting from any ideas, methods, instructions or products referred to in the content.